Biomech Model Mechanobiol (2010) 9:1–17
DOI 10.1007/s10237-009-0154-5

ORIGINAL PAPER

A multiscale model for red blood cell mechanics

Dirk Hartmann

Received: 26 September 2008 / Accepted: 24 March 2009 / Published online: 7 May 2009

Abstract The objective of this article is the derivation of a continuum model for mechanics of red blood cells via multiscale analysis. On the microscopic level, we consider realistic discrete models in terms of energy functionals defined on networks/lattices. Using concepts of Γ-convergence, convergence results as well as explicit homogenisation formulae are derived. Based on a characterisation via energy functionals, appropriate macroscopic stress–strain relationships (constitutive equations) can be determined. Further, mechanical moduli of the derived macroscopic continuum model are directly related to microscopic moduli. As a test case we consider optical tweezers experiments, one of the most common experiments to study mechanical properties of cells. Our simulations of the derived continuum model are based on finite element methods and account explicitly for membrane mechanics and its coupling with bulk mechanics. Since the discretisation of the continuum model can be chosen freely, rather than it is given by the topology of the microscopic cytoskeletal network, the approach allows a significant reduction of computational efforts. Our approach is highly flexible and can be generalised to many other cell models, also including biochemical control.

Keywords Biomechanics · Red blood cells · Cytoskeleton · Multiscale modelling · Effective properties

This work was supported by the German Science Foundation through the International Graduate College 710: "Complex Processes: Modeling, Simulation and Optimization".

D. Hartmann (✉)
Center for Modelling and Simulation in the Biosciences (BIOMS), University of Heidelberg, BQ 00 21 BIOQUANT, Im Neuenheimer Feld 267, 69120 Heidelberg, Germany
e-mail: dirk.hartmann@bioquant.uni-heidelberg.de; Dirk.Hartmann@iwr.uni-heidelberg.de

1 Introduction

Biological systems are among the most complicated ones studied in the natural sciences. The investigation of mechanical issues in biological systems has a long tradition dating back to the seminal book *On Growth and Form* by Thompson (1917).

From a mechanist's point of view, cells are well characterised by a continuum theory on a macroscopic level, e.g. cells are often described by hyperelastic (or Green elastic) materials. On a microscopic level, e.g. on the scale of the cytoskeleton of a cell, continuous descriptions are often not appropriate and discrete descriptions typically in terms of energy functionals are preferable. At the same time, different physical concepts like entropic forces have to be considered. On the one hand microscopic models allow an approach considering as many details as possible. On the other hand, often, biologically interesting length scales are not accessible by microscopic models due to limited computational capacities.

The aim of this article is the extension of multiscale techniques to biomechanical applications. These techniques allow the rigorous upscaling of appropriate basic microscopic descriptions to macroscopic continuum models which inherit the microscopic properties. Using concepts from Γ-convergence (Dal Maso 1993; Braides 2002), the gap between those two descriptions can be closed systematically: based on a microscopic description, an explicit continuous macroscopic description can be derived in terms of energy functionals. From the latter, stress–strain relationships used in the framework of hyperelasticity can be calculated, which allows a description in terms of mass and linear momentum conservation.

In this article, we generalise the approach of Alicandro and Cicalese (2004) to more general energies, e.g. describing the

mechanical properties of the membrane skeleton of red blood cells. To our knowledge this is the first approach that systematically derives a continuum mechanical model for red blood cells based on discrete molecular models. A simple heuristic approach linking mechanical properties of a thin shell with finite thickness with a discrete molecular model can be found in Dao et al. (2006).

The continuum model derived in this article considers the membrane as a hypersurface with mechanical properties resisting bending and stretching. Membrane mechanics can be coupled with the cytosol (a simple fluid) allowing the calculation of energy minimising shapes (observed shapes), as well as an extension to more complex setups where dynamics play a crucial role. Our model is challenged by the quantitative comparison of simulations of the derived macroscopic model with microscopic simulations as well as optical tweezers experiments, one of the most common experiments in biophysics. To do so, an appropriate finite element framework is set up which is implemented in GASCOIGNE (Becker et al. 2009). Simulations of the macroscopic continuum model show a good qualitative and quantitative agreement with the microscopic approach and experiments..

The model as well as the simulation approach can be extended easily to include much more details, e.g. chemical processes controlling the membrane elasticity of the red blood cell. Using the homogenisation approach allows a significant reduction of computational complexity. Considering a realistic number of filaments in a discrete microscopic model, the system is hardly solvable. However, using a continuum approach, finite element methods allow the choice of relatively coarse discretisations speeding up simulations. The efficiency of computations for continuum models can be further increased by appropriate mesh refinement strategies. Another significant advantage of continuum models is that they can be easily coupled with reaction–diffusion equations, which are typically used to model biochemical reaction networks in cells. This allows a straightforward approach investigating interactions between mechanics and biochemistry. And last, but not least, continuum models are usually more accessible to mathematical analysis than discrete models.

The structure of the article is as follows: First we review in Sect. 1.1, biomechanics of red blood cells as well as optical tweezers experiments. In Sect. 2, we introduce a realistic static microscopic model for optical tweezers experiments based on existing microscopic approaches. A corresponding static continuum model is then systematically derived in Sect. 3. Using a variational approach allows us to determine energy minimisers via relaxation. To do so a corresponding continuum mechanical model in terms of mass and liner momentum conservation is set up for optical tweezers experiments (Sect. 4). Finally, we introduce in Sect. 5 an appropriate numerical approach for solving the derived model and close with a discussion of the results in Sect. 6.

1.1 Biology and mechanics of red blood cells

Red blood cells (RBC) have a simple structure and therefore often serve as model systems for the development of theoretical and experimental methods in biophysics. Under physiological conditions, a normal human RBC in an unstressed state assumes a biconcave discoid shape approximately 8μm in diameter (Evans and Skalak 1980):

$$z = R\sqrt{1-(x^2+y^2)/R^2}[c_0 + c_1(x^2+y^2)/R^2 + c_2(x^2+y^2)^2/R^4], \quad (1)$$

where $R = 3.91\,\mu\text{m}$, $c_0 = 0.1035805$, $c_1 = 1.001270$, and $c_2 = -0.561381$. The nucleus and other organelles that are present in RBCs during their development are expelled before and shortly after the cells are released into the circulatory system, leaving the mature cells with no internal structural components other than the membrane-associated spectrin cytoskeleton (Boal 2002), a quasi two-dimensional (2D) network (Fig. 1). Basic building blocks of the spectrin network are 200 nm long spectrin tetramers (edges) which crosslink the junctional complexes of actin (vertexes). The average length between two vertexes is 80 nm (Liu et al. 1987). Hence, the end-to-end distance of spectrin tetramers is significantly smaller than their contour length, which strongly underlines that mechanics are due to entropic effects. According to Liu et al. (1987), there are over 80% degree-6 vertexes in spectrin networks extracted from healthy human RBCs, which suggest a relative regular hexagonal structure of the spectrin network (c.f. Fig. 1). However, recent experiments indicate that the network might be more disordered with a significant lower average vertex degree (Li et al. 2005).

Functional actin complexes are affected by ATP, which is usually present in RBCs, by inducing spectrin–actin dissociations (Gov and Safran 2005). Creation and motion of such defects allows the network to rearrange constantly. Therefore, it is postulated that the spectrin vertices of RBCs behave like a liquid on large time scales. Thus dynamics would allow a relaxation of the in-plane shear elastic energy (Li et al. 2005). However, for periods of around 30 min and temperatures up to 37°C large cytoskeletal deformations have shown to be stable (Lee et al. 1999), i.e. during this timescale RBCs can manifest large shear.

One of the most common experiments to study mechanics of RBCs as well as other cell types are optical tweezers experiments (Fig. 1) (Hénon et al. 1999; Mills et al. 2004). Using focused laser beams, optical tweezers allow the application of forces in the range of pico Newtons to dielectric microbeads. Since forces applied to the optical tweezers can be determined quite well, the experiments allow the estimation of involved mechanical moduli. Usually, the deformation rate is faster than the relaxation rate of stresses, such that relaxation can be neglected (Li et al. 2005).

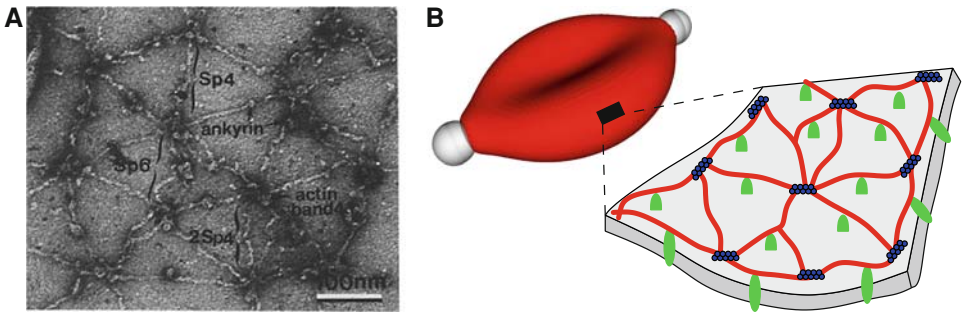

Fig. 1 **a** Spread membrane skeleton examined by negative-staining electron microscopy. It clearly shows the RBC's hexagonal lattice of junctional complexes (reprinted from Liu et al. (1987), ©1987 Rockefeller University Press). **b** Schematic presentation of a red blood cell between optical tweezers (according to Hansen et al. (1997), ©1997 Biophysical Society)

1.2 Models of red blood cells

Quite a variety of models for mechanics of RBCs are found in the literature. These can be divided into two classes: microscopic molecular based models (i.e. discrete models) (e.g. Hansen et al. 1997; Discher et al. 1998; Li et al. 2005; Noguchi and Gompper 2005), and macroscopic continuum models (e.g. Evans and Skalak 1980; Lim et al. 2002; Mills et al. 2004; Dao et al. 2003, 2006; Pozrikidis 2003a). Among them, we can distinguish solely static models (Discher et al. 1998), i.e. models based on energy minimisation, or dynamic models (Noguchi and Gompper 2005), mainly concerned with RBCs embedded in fluid flow. Further, we can distinguish between models which treat the membrane as a 2D hypersurface (Discher et al. 1998) and those which treat it as a shell (Dao et al. 2003) with a small but finite thickness. The list of references given here is by no means complete, for a more detailed list we refer to Hartmann (2007).

The objective of this paper is to show how the different models can be rigorously linked. Here, we restrict ourselves to a slightly simplified variant of the molecular based static model proposed by Boey et al. (1998) and Discher et al. (1998). A corresponding continuum model is derived in Sect. 3 using Γ-convergence. The static continuum model can be linked to a dynamic continuum model using a variational approach, as shown in Sect. 4.

2 Static molecular based model

The major advantage of discrete models is their simplicity, which allows straightforward numerical schemes, e.g. Monte Carlo methods. Most microscopic models go back to the work of Boey et al. (1998) and Discher et al. (1998) considering a micropipette aspiration experiment. Their approach has been also extended to optical tweezers experiments (Li et al. 2005). Let us review the original model in the case of an optical tweezers experiment using a slightly different notation adopted to our setup:

Model 1 The stationary shape of the RBC in an optical tweezers minimises the discrete free energy

$$F_\varepsilon(\{\boldsymbol{\chi}_n\}) = F_{\varepsilon,\text{tweezers}} + F_{\varepsilon,\text{in-plane}} + F_{\varepsilon,\text{bending}} + F_{\varepsilon,\text{surface}} + F_{\varepsilon,\text{volume}}.$$

Here ε is the typical length scale of the spectrin network. The degrees of freedom of the model are the actin vertex coordinates $\{\boldsymbol{\chi}_n = \boldsymbol{\chi}(\boldsymbol{X}_n)\}_{n\in 1,\dots,N}$ (see Fig. 1), where $\boldsymbol{X}_n$ is the position of a network vertex in the reference configuration. Its motion / deformation is thus given by the function

$$\boldsymbol{x} = \boldsymbol{\chi} : \mathbb{R}^3 \ni \boldsymbol{X} \mapsto \boldsymbol{\chi}(\boldsymbol{X}) \in \mathbb{R}^3.$$

Since we are interested in mechanics, we will restrict ourselves to deformations preserving the orientation.

Based on the observations of Liu et al. (1987), Discher and co-workers propose to model the mechanics of RBCs using a quasi-2D network with hexagonal symmetry (including 12 topological defects, which are needed to cover a sphere with a hexagonal net). This approach has been generalised by Li et al. (2005) to more general networks. In this section, we will not rely on a special geometry; however in Sect. 3 we will restrict ourselves to a purely hexagonal geometry in order to derive a corresponding continuum model, which can be explicitly specified.

All energies considered in Model 1 are non-negative, apart from $F_{\varepsilon,\text{tweezers}}$ modelling the effect of optical tweezers. Let us assume that N_{tweezers} actin vertex coordinates are bound to the microbeads of the optical tweezers on both sides. Therefore, they experience a force corresponding to the energy:

$$F_{\varepsilon,\text{tweezers}}(\{\boldsymbol{\chi}_n\}) = -\sum_{\boldsymbol{X}_i \text{ bound}} \frac{1}{N_{\text{tweezers}}} (\boldsymbol{\chi}(\boldsymbol{X}_i) - \boldsymbol{X}_i) \cdot \boldsymbol{f}_{\text{tweezers}},$$

where $\boldsymbol{f}_{\text{tweezers}}$ is the force applied by the optical tweezers.

The dominant term of the membrane energy in the context of large deformations, e.g. in optical tweezers experiments,

is the in-plane free energy $F_{\varepsilon,\text{in-plane}}$ of the membrane-bound cytoskeleton:

$$F_{\varepsilon,\text{in-plane}}(\{\boldsymbol{\chi}_n\}) = \sum_{\text{edges}} L^2_{(m,n)} \frac{\sqrt{3}}{2} \tilde{V}_{\text{WLC}}\left(\frac{\mathcal{L}^2_{(m,n)}}{L^2_{(m,n)}}\right) + \sum_{\text{faces}} 2A_{(l,m,n)} \frac{C}{(\mathcal{A}_{(l,m,n)}/A_{(l,m,n)})^q + \eta}, \tag{2}$$

where $\mathcal{L}_{(l,m)} = |\boldsymbol{\chi}_m - \boldsymbol{\chi}_l|$ is the length of the spectrin link / edge connecting vertexes l, m and $\mathcal{A}_{(l,m,n)} = |(\boldsymbol{\chi}_m - \boldsymbol{\chi}_l) \times (\boldsymbol{\chi}_n - \boldsymbol{\chi}_l)|/2$ is the area of the triangular face enclosed by the spectrin links (l,m), (m,n), (n,l) in the deformed state. $L_{(l,m)} = O(\varepsilon)$ and $A_{(l,m,n)} = O(\varepsilon^2)$ are the edge lengths and face areas in the reference coordinate system. The different terms in (2) are explained in detail below.

Let us rewrite the relative lengths $\mathcal{L}_{(l,m)}/L_{(l,m)}$ and areas $\mathcal{A}_{(l,m,n)}/A_{(l,m,n)}$ used in formula (2) in terms of discrete finite difference quotients $D^{\boldsymbol{\xi}}_L \boldsymbol{\chi}(\boldsymbol{X}) \equiv (\boldsymbol{\chi}(\boldsymbol{X}_l + L\boldsymbol{\xi}) - \boldsymbol{\chi}(\boldsymbol{X}))/L$ (in direction of the vector $\boldsymbol{\xi}$), which will facilitate our mathematical analysis in Sect. 3:

$$\begin{aligned} \frac{\mathcal{L}_{(l,m)}}{L_{(l,m)}} &= \frac{|\boldsymbol{\chi}(\boldsymbol{X}_l + L_{(l,m)}\boldsymbol{\xi}_{(\boldsymbol{l},\boldsymbol{m})}) - \boldsymbol{\chi}(\boldsymbol{X}_l)|}{L_{(l,m)}} \\ &= |D^{\boldsymbol{\xi}_{(l,m)}}_{L_{(l,m)}} \boldsymbol{\chi}(\boldsymbol{X}_l)|, \end{aligned} \tag{3}$$

$$\begin{aligned} \frac{\mathcal{A}_{(l,m,n)}}{A_{(l,m,n)}} &= \det\left(D^{\boldsymbol{\xi}_{(l,m)}}_{L_{(l,m)}} \boldsymbol{\chi}(\boldsymbol{X}_l) \otimes D^{\boldsymbol{\xi}_{(l,n)}}_{L_{(l,n)}} \boldsymbol{\chi}(\boldsymbol{X}_l)\right) \\ &= J_{(l,m,n)}(\boldsymbol{\chi}(\boldsymbol{X}_l)), \end{aligned} \tag{4}$$

where $\boldsymbol{\xi}_{(l,m)} = (\boldsymbol{X}_m - \boldsymbol{X}_l)/|\boldsymbol{X}_m - \boldsymbol{X}_l|$ is the unit vector pointing from vertex $\boldsymbol{X}_l$ to the vertex $\boldsymbol{X}_m$ in the undeformed coordinate system. $J_{(l,m,n)}(\boldsymbol{\chi}(\boldsymbol{X}_l))$ is the discrete Jacobian corresponding to the triangle spanned by the vertexes l, m, and n. Since we consider only orientation preserving deformations $J_{(l,m,n)}(\boldsymbol{\chi}(\boldsymbol{X}_l))$ and equivalently $\mathcal{A}_{(l,m,n)}/A_{(l,m,n)}$ are always positive.

The first term in (2) is the entropic energy stored in the spectrin links. Discher and co-workers assume that the energy is given by the *worm-like chain* model introduced by Marko and Siggia (1995), which is based on experiments with DNA:

$$L^2 \frac{\sqrt{3}}{2} V_{\text{WLC}}\left(\frac{\mathcal{L}^2}{L^2}\right) = \frac{k_B T}{4p\mathcal{L}_{\max}} \frac{\mathcal{L}^2(2\mathcal{L} - 3\mathcal{L}_{\max})}{(\mathcal{L} - \mathcal{L}_{\max})}. \tag{5}$$

Since $\lim_{\mathcal{L}\to\mathcal{L}_{\max}} V_{\text{WLC}}(\mathcal{L}^2/L^2) = \infty$, we consider here a pth-order Taylor-expansion $\tilde{V}_{\text{WLC}}$ of V_{WLC} around the rest state $\mathcal{L} = L$ due to mathematical restrictions (as we will see below). Hence, V_{WLC} is a positive super-linearly growing function with p-growth, i.e. it satisfies the following growth condition

$$c_1(|z|^p - 1) \le \tilde{V}_{\text{WLC}}(z^2) \le c_2(|z|^p + 1) \tag{6}$$

for constant $c_1, c_2 \in \mathbb{R}^+$ $1 \le p < \infty$. Dimensional analysis reveals that $\tilde{V}_{\text{WLC}}(\mathcal{L}^2/L^2)$ is an energy density, respectively $\tilde{V}_{\text{WLC}}(\mathcal{L}/L)$.

Considering only $\tilde{V}_{\text{WLC}}$ in (2), the minimum of $F_{\varepsilon,\text{in-plane}}$ corresponds to a collapsed network. However, due to repulsive forces of steric interactions (i.e. entropic forces) the network does not collapse: The end-to-end distance of spectrin filaments is much smaller than their contour length. Hence, spectrin fibres are polymer coils with a non-negligible width leading to repulsion. Therefore, the second sum is introduced into the model. It is of a phenomenological origin and accounts for steric interactions (Discher et al. 1998). $C > 0$ and $q > 0$ are constants, typically the case $q = 1$ is adopted (Discher et al. 1998; Li et al. 2005). Due to mathematical restrictions (see below) the constant $\eta > 0$ is introduced to ensure that the contribution of the repulsive forces is bounded. Dimensional analysis shows that $C/[(\mathcal{A}_{(l,m,n)}/A_{(l,m,n)})^q + \eta]$ is an energy density.

The introduction of the regularisation of repulsive steric interactions in (2), i.e. the introduction of $\eta > 0$, as well as the restriction to Taylor expansions of V_{WLC} is necessary to obtain rigorous convergence results following the work of Alicandro and Cicalese (2004). Without this regularisation our approach yields only formal results which would still needed to be verified by mathematical analysis.

Due to the fluid character of the lipid bilayer it cannot sustain shear–stress; nevertheless, it possesses a bending stiffness and a large compressional stiffness. Often, it is assumed to be incompressible. Since the building blocks of the lipid bilayer are much smaller than the spectrin links, the resistance to bending of the lipid bilayer is well described by continuum models, e.g. the Canham and Helfrich functional (Canham 1970; Helfrich 1973):

$$F_{\text{Canham–Helfrich}} = \frac{\kappa}{2} \int_\Gamma (H - H_0)^2 \mathrm{d}\mu + \kappa_g \int_\Gamma K \,\mathrm{d}\mu \tag{7}$$

with cell membrane Γ, bending elasticity moduli κ, κ_g, mean curvature $H = C_1 + C_2$, Gauss curvature $K = C_1 C_2$, principal curvatures C_1, C_2, and the constant H_0, which represents the spontaneous curvature. The last term in (7) can be neglected, since due to the Gauss–Bonnet theorem the integral is constant for a given topology (We allow only variations over a fixed topology). The Canham–Helfrich functional is well-established for intermediate surface curvatures based on molecular dynamic simulations (den Otter and Briels 2003) on the one hand as well as experiments (Steltenkamp et al. 2006) on the other hand. It is a sufficient approximation considering optical tweezers experiments, which exhibit relative mild curvatures.

Therefore the microscopic models proposed by Discher et al. (1998) and Li et al. (2005) rely on the Canham–Helfrich energy, although more complex approaches can be found

in the literature, e.g. considering non-local bending energies (Seifert et al. 1991; Bozic et al. 1992; Miao et al. 1994; Mukhopadhyay et al. 2002). To work with a fully discrete approach, Discher and co-workers discretised the Canham–Helfrich model (7) using network vertex-coordinates as degrees of freedom yielding a discrete free energy $F_{\varepsilon,\text{bending}}(\{\boldsymbol{\chi}_n\})$. For the discrete formulation we refer to the original paper Discher et al. (1998). In the following we will work directly with the continuum description (7), which is possible since Γ-convergence is stable to continuous perturbations (Braides 2001). Of course, also more complex models for membrane mechanics, e.g. non-local bending energies, can be included in our approach. Here, we however rely on the somewhat simpler Canham–Helfrich energy to allow an exact quantitative comparison between simulations of the microscopic model and the upscaled macroscopic model. Precise measurements of bilayer bending elasticity can be found in the literature (Mohandas and Evans 1994; Heinrich and Waugh 1996; Hwangand and Waugh 1997; Rawicz et al. 2000; Scheffer et al. 2001).

The non-physical energies $F_{\varepsilon,\text{volume}}$ and $F_{\varepsilon,\text{surface}}$ account phenomenologically for the incompressibility of the cytosol and of the lipid bilayer:

$$F_{\varepsilon,\text{volume}}(\{\boldsymbol{\chi}_n\}) = k_{\text{volume}}(|\mathcal{V}_{\text{cell}}| - \mathcal{V}_{\text{desired}})^2,$$
$$F_{\varepsilon,\text{surface}}(\{\boldsymbol{\chi}_n\}) = k_{\text{surface}}(|\mathcal{A}_{\text{cell}}| - \mathcal{A}_{\text{desired}})^2,$$

where the total area of the cell is given by $\mathcal{A}_{\text{cell}} = \sum_{\text{faces}} \mathcal{A}_{(l,m,n)}$ and the total volume by $\mathcal{V}_{\text{cell}}$. The latter can be directly related to the areas $\mathcal{A}_{(l,m,n)}$, since the divergence theorem $|\Omega| = \frac{1}{3}\int_{\partial\Omega}(\boldsymbol{x}\cdot\boldsymbol{n})\mathrm{d}\mu$ must hold. k_{volume} and k_{surface} are constants.

According to the adopted hypothesis, the stationary shape of the RBC, e.g. stretched by optical tweezers, minimises the free energy. Boey et al. (1998); Discher et al. (1998) use Monte Carlo schemes for energy minimisation and Li et al. (2005) use coarsegrained molecular dynamics to determine the energy minimum. Both start with a given reference shape and let the energy relax until a minimum is reached. Using these approaches, the experimentally observed shapes are recovered.

The choice of an appropriate reference shape (initial or rest shape) is however subtle, since the computed shapes depend usually on the chosen reference shape (Li et al. 2005). Li et al. (2005) have invoked the physical hypothesis that the spectrin network undergoes constant remodelling to always relax the in-plane shear elastic energy to zero at some slow characteristic time scale. Therefore they suggest to use an initial shape which minimises the energy $F_{\varepsilon,\text{bending}} + F_{\varepsilon,\text{surface}} + F_{\varepsilon,\text{volume}}$ (in-plane energy is neglected). Using this approach the biconcave shape (1) is recovered (Li et al. 2005) (see also Sect. 5.3.1).

Starting from this reference shape the energy minimum of the full Model 1 is determined (see Fig. 7). For computations as well as a more detail we refer to the original paper (Li et al. 2005).

3 From molecular based to continuum models

Different static continuum models in terms of energy functionals for mechanics of RBCs can be found in the literature (Mukhopadhyay et al. 2002; Kuzman et al. 2004; Lim et al. 2002). These have the same structure as the microscopic model considered above, but they are however generally of a heuristic type.

In the following, we derive systematically a continuous energy functional F for the mechanics of RBCs based on the microscopic model F_ε given in Model 1. Because we are generally interested in deformations with minimal energies, Γ-convergence is an appropriate framework.

In the following we will concentrate on the energies $F_{\varepsilon,\text{bending}} + F_{\varepsilon,\text{in-plane}}$, since $F_{\varepsilon,\text{surface}}$, $F_{\varepsilon,\text{volume}}$ are of a non-physical type and $F_{\varepsilon,\text{tweezers}}$ has an obvious continuous counterpart. Further, we replace $F_{\varepsilon,\text{bending}}$ with $F_{\text{Canham–Helfrich}}$, i.e. expression (7). Since Γ-convergence is stable with respect to continuous perturbations (Braides 2002), it is sufficient to restrict ourselves to $F_{\varepsilon,\text{in-plane}}$, which represents the energy contribution of the discrete spectrin cytoskeleton / membrane skeleton.

The free energy $F_{\varepsilon,\text{in-plane}}$ is independent of deformations perpendicular to the membrane. Therefore we consider only the 2D tangent space of the membrane for the sake of simplicity. Further, we restrict our analysis to 2D networks with hexagonal symmetry (Fig. 2) in order to find an explicit expression for the continuum functional and not only abstract convergence results. Let us introduce the considered networks

$$\varepsilon\mathcal{G} \cap \Omega$$

with

$$\mathcal{G} = \{\boldsymbol{X} \in \mathbb{R}^2 : \boldsymbol{X} = \mu_1\boldsymbol{g}_1 + \mu_2\boldsymbol{g}_2 \text{ with } \mu_i \in \mathbb{Z}\}, \tag{8}$$

$\boldsymbol{g}_1 = (1,0)$, $\boldsymbol{g}_2 = (1/2, \sqrt{3/4})$, and $\Omega \subset \mathbb{R}^2$ open and bounded. Here, ε is the typical length scale of the network. The basic building block of the network is a unit cell as illustrated in Fig. 2 with links $\mathcal{G}^{\boldsymbol{\xi}} = \{\boldsymbol{\xi}_i\}$ and triangles $\mathcal{G}^{\triangle} = \{\triangle_i\}$. Since we restrict ourselves to the tangent space, the deformation of network vertexes $\boldsymbol{X} \in \varepsilon\mathcal{G} \cap \Omega$ is given by

$$\boldsymbol{x} = \boldsymbol{\chi} : \varepsilon\mathcal{G} \cap \Omega \ni \boldsymbol{X} \mapsto \boldsymbol{\chi}(\boldsymbol{X}) \in \mathbb{R}^2,$$

which should be orientation preserving, as discussed above.

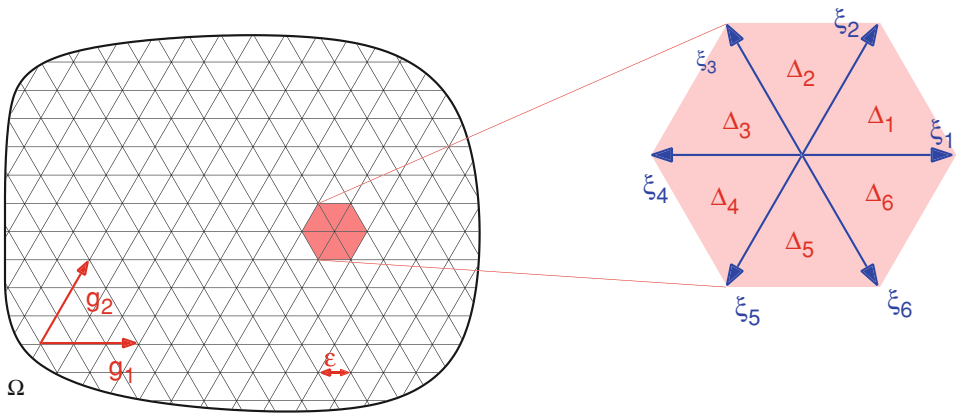

Fig. 2 Abstraction of the 2D membrane skeleton of a red blood cell spread on a flat 2D domain Ω shown in Fig. 1

Let us rewrite (2) as follows:

$$F_{\varepsilon,\text{in-plane}}(\boldsymbol{\chi},\Omega) = \sum_{\substack{\boldsymbol{X}\in \text{vertexes}\\ \text{in}\,\Omega}} \left[\frac{1}{2} \sum_{\substack{\boldsymbol{\xi}\in \text{edges in}\,\Omega\\ \text{connected to}\,\boldsymbol{X}}} \varepsilon^2 \frac{\sqrt{3}}{2} \tilde{V}_{\text{WLC}} \left(\left(D_\varepsilon^{\boldsymbol{\xi}} \boldsymbol{\chi}(\boldsymbol{X}) \right)^2 \right) + \frac{1}{3} \sum_{\substack{\triangle\in \text{faces in}\,\Omega\\ \text{connectedto}\,\boldsymbol{X}}} \varepsilon^2 \frac{\sqrt{3}}{2} \frac{C}{(J_{\varepsilon\triangle}(\boldsymbol{\chi}(\boldsymbol{X})))^q + \eta} \right], \tag{9}$$

where $D_\varepsilon^{\boldsymbol{\xi}} \boldsymbol{\chi}(\boldsymbol{X})$ is the discrete finite difference quotient (3), i.e. the relative length change of the edge in the deformed configuration, and $J_{\varepsilon\triangle}(\boldsymbol{\chi}(\boldsymbol{X}))$ is the discrete Jacobian (4), i.e. the relative face area change in the deformed configuration. The factor $1/2$ in front of the pair interactions accounts for the fact that each interaction is counted twice. Similarly a factor $1/3$ accounts for the multiple counting of steric interactions. The scaling $\varepsilon^2\sqrt{3}/2$ is the natural geometrical scaling.

Neglecting steric interaction, i.e. choosing $C = 0$ and thus considering only pair-interactions, $F_{\varepsilon,\text{in-plane}}$ is a special case of free energies describing atomistic interactions in crystal lattices. Such energies have been studied in several works (Alicandro and Cicalese 2004; Braides 2001) using Γ-convergence as well as other techniques (Berezhnyy and Berlyand 2006; Schmidt 2008).

A constructive proof based on the concept of Γ-convergence, calculating the lim inf and lim sup inequalities directly, is relatively straightforward in 1D (Braides 2001). In higher dimensions, the direct calculation of the lim inf inequality is, however, highly non-trivial, unless the problem can be reduced to several 1D problems, e.g. in the direction of the coordinate axes. Due to the steric interaction energies, involving multiple dimensions, such a reduction is not possible in our setup.

Considering crystal lattices Alicandro and Cicalese (2004) use a more abstract approach based on Γ-convergence results from the theory of homogenisation of integrals (Braides and Defranceschi 1998). This abstract approach allows to prove the existence of appropriate continuum limit energy functionals. Considering periodic microscopic geometries, the continuum functionals can be characterised indirectly as a limit of discrete functionals on simple rectangular domains.

Since the steric interaction energies in (2) are positive and bounded the proof of Alicandro and Cicalese (2004) needs basically no modification. Therefore, we review here only the corresponding results. Using convexity of the functional, we then derive an appropriate cell problem, i.e. a homogenisation formula.

3.1 Existence

To consider possible minimisers $\boldsymbol{\chi}$ of (9) for arbitrary ε within one function space, we identify the discrete maps $\boldsymbol{\chi} : \varepsilon\mathcal{G} \cap \Omega \to \mathbb{R}^2$ with maps $\boldsymbol{\chi} : \Omega \to \mathbb{R}^2$ constant on each cell of the lattice. Therefore, let us introduce the following function spaces:

$$\mathcal{F}_\varepsilon(\Omega) \equiv \Big\{ \boldsymbol{u} : \Omega \to \mathbb{R}^2 : \text{ for any } \boldsymbol{X} \in \varepsilon\mathcal{G}, \boldsymbol{u} \text{ is constant on } \{\boldsymbol{Y} \in R^2 : \boldsymbol{Y} = \boldsymbol{X} + \mu_1\boldsymbol{g}_1 + \mu_2\boldsymbol{g}_2, 0 \le \mu_i < \varepsilon\} \Big\},$$
$$\mathcal{F}_{\varepsilon,\phi}(\Omega) \equiv \{ \boldsymbol{u} \in \mathcal{F}_\varepsilon(\Omega) : \boldsymbol{u}(\boldsymbol{X}) = \phi(\boldsymbol{X}) \text{ if } d(\boldsymbol{X}, \partial\Omega) < 1 \}.$$

Of course other embeddings, e.g. assuming piecewise linear functions, can be considered equivalently.

Theorem 1 *For every sequence (ε_j) of positive real numbers converging to 0, there exists a sub-sequence (ε_{j_k}) and a continuous quasi-convex function $\Psi : \mathbb{R}^{2\times 2} \to [0,\infty)$ satisfying*

$$c(|\mathbf{M}|^p - 1) \le \Psi(\mathbf{M}) \le C(|\mathbf{M}|^p + 1)$$

with $0 < c < C$, such that $(F_{\varepsilon_{j_k},\text{in-plane}}(\cdot,\cdot))$ given in (9) Γ-converges with respect to the $L^p(\Omega;\mathbb{R}^2)$-topology to $F_{\text{in-plane}} : L^p(\Omega;\mathbb{R}^2) \times \{A \subset \Omega : A \text{ open}\} \to [0,\infty]$ defined as

$$F_{\text{in-plane}}(\boldsymbol{\chi}, A) = \begin{cases} \int_A \Psi(\nabla_{\mathbf{x}}\boldsymbol{\chi})\mathrm{d}\mu & \text{if } \boldsymbol{\chi} \in W^{1,p}(A;\mathbb{R}^2) \\ \infty & \text{otherwise.} \end{cases}$$

Here, $W^{1,p}(A;\mathbb{R}^2)$ are standard Sobolev spaces (Alt 2002).

As already mentioned Alicandro and Cicalese (2004) consider energies of the type (9) without steric interactions, i.e. $C \equiv 0$. They show that the upper and lower Γ-limits of these functionals defined on pairs function-set are inner-regular increasing set functions. This allows the use of a corresponding compactness and integral representation result (Braides and Defranceschi 1998). Considering the case $C \neq 0$ the arguments can be repeated. The pair interactions in (9) fulfil the required growth conditions, c.f. growth condition (6), and the repulsive energy of steric interactions in (9) is bounded, such that the proof of Theorem 1 goes along the lines of the original proof.

The embedding of $W^{1,p}(\Omega;\mathbb{R}^2)$ to $L^p(\Omega;\mathbb{R}^2)$ is compact using the standard definition of L^p spaces (Alt 2002). Hence, Theorem 1 implies also the convergence of minimisers to a minimiser of the limit functional. Theorem 1 considers an unconstrained Γ-limit.

However, often one is interested in problems with prescribed boundary conditions. Corresponding convergence results with restrictions to $\boldsymbol{\chi} \in \mathcal{F}_{\varepsilon,\boldsymbol{\phi}}$, and accordingly $\boldsymbol{\chi} - \boldsymbol{\phi} \in W_0^{1,p}(\Omega;\mathbb{R}^2)$, can be proven. Here, we use the standard definition for $W_0^{1,p}(\Omega;\mathbb{R}^2)$, i.e. Sobolev functions of the space $W^{1,p}(\Omega;\mathbb{R}^2)$ with a vanishing trace on the boundary of Ω (Alt 2002). Similar results hold also for periodic boundary conditions. For more details, we refer to the work of Alicandro and Cicalese (2004).

3.2 Homogenisation

Let us first define a rhombus which is spanned by N times the vector $\boldsymbol{g}_1$ and N times the vector $\boldsymbol{g}_2$, c.f. definition (8):

$$Q_N = \{\boldsymbol{X} : \boldsymbol{X} = \mu_1\boldsymbol{g}_1 + \mu_2\boldsymbol{g}_2 \quad \text{with} 0 \leq \mu_i < N, i = 1, 2\}.$$

Minor modifications of the approach of Alicandro and Cicalese (2004), yield the following homogenisation result:

Theorem 2 *For every sequence (ε_j) of positive real numbers converging to 0, the sequence $(F_{\varepsilon_j,\text{in-plane}})$ given in (9) Γ-converges with respect to the $L^p(\Omega;\mathbb{R}^2)$-topology to $F_{\text{in-plane}} : L^p(\Omega;\mathbb{R}^2) \times \{A \subset \Omega : A \text{ open}\} \to [0,\infty]$ defined as*

$$F_{\text{in-plane}}(\boldsymbol{\chi}, A) \equiv \begin{cases} \int_A \Psi_{\text{hom}}(\nabla_{\mathbf{x}}\boldsymbol{\chi})\mathrm{d}\mu & \text{if } \boldsymbol{\chi} \in W^{1,p}(A;\mathbb{R}^2) \\ \infty & \text{otherwise,} \end{cases}$$

where the integrand $\Psi : \mathbb{R}^{2\times 2} \to [0,\infty)$ satisfies the rescaled homogenisation formula

$$\Psi_{\text{hom}}(\mathbf{M}) \equiv \lim_{N\to\infty} \frac{1}{N^2} \min\left\{F_{1,\text{in-plane}}(\boldsymbol{\chi}, Q_N) : \boldsymbol{\chi} = \mathbf{M}\cdot\boldsymbol{X} + \boldsymbol{u} \right. \\ \left. \text{with } (N-2)\text{-periodic } \boldsymbol{u} \in \mathcal{F}_1(Q_N)\right\} \tag{10}$$

with $F_{1,\text{in-plane}}$ defined in (9).

An analogous result holds also in the case of Dirichlet or periodic boundary conditions with the same characterisation of Ψ_{hom}. Above, $(N-2)$-periodic functions $\boldsymbol{u}$, i.e. $\boldsymbol{u}(\boldsymbol{X} + (N-2)\boldsymbol{g}_1) = \boldsymbol{u}(\boldsymbol{X})$ as well as $\boldsymbol{u}(\boldsymbol{X} + (N-2)\boldsymbol{g}_2) = \boldsymbol{u}(\boldsymbol{X})$, are considered to ensure that the discrete derivative of the perturbation on the boundary is zero.

3.3 Cell problem

The homogenisation formula (10) in Theorem 2 is given as a minimisation problem over a growing rectangle Q_N $(N \to \infty)$. Since the contribution from pair as well as steric interactions are convex the homogenisation formula can be reduced to a cell problem, i.e. a homogenisation formula:

Theorem 3 *For every sequence (ε_j) of positive real numbers converging to 0, the sequence $(F_{\varepsilon_j,\text{in-plane}})$ given in (9) Γ-converges with respect to the $L^p(\Omega;\mathbb{R}^2)$-topology to $F_{\text{in-plane}} : L^p(\Omega;\mathbb{R}^2) \times \{A \subset \Omega : A \text{ open}\} \to [0,\infty]$ defined as*

$$F_{\text{in-plane}}(\boldsymbol{\chi}, A) \equiv \begin{cases} \int_A \Psi(\nabla_{\mathbf{x}}\boldsymbol{\chi})\mathrm{d}\mu & \text{if } \boldsymbol{\chi} \in W^{1,p}(A;\mathbb{R}^2) \\ \infty & \text{otherwise,} \end{cases}$$

where the integrand $\Psi : R^{2\times 2} \to [0,\infty)$ is given by the following problem on a unit-cell

$$\Psi \equiv \frac{1}{2}\sum_{i=1,\ldots,6} \tilde{V}_{WLC}\left(\boldsymbol{\xi}^T\cdot(\nabla_{\mathbf{x}}\boldsymbol{\chi})^T\cdot(\nabla_{\mathbf{x}}\boldsymbol{\chi})\cdot\boldsymbol{\xi}\right) \\ + 2\frac{C}{(\det(\nabla_{\mathbf{x}}\boldsymbol{\chi})^q + \eta)} \tag{11}$$

with vectors $\boldsymbol{\xi}_i \in \mathcal{G}^{\boldsymbol{\xi}}$ $(|\boldsymbol{\xi}_i| = 1)$ corresponding to the spectrin edges in the undeformed unit cell (c.f. Fig. 2).

Proof For simplicity, we split the proof into two parts: (a) the case $C \equiv 0$ and (b) $\tilde{V}_{\text{WLC}} \equiv 0$. For all N, we show that in both cases, $\boldsymbol{\chi} = \mathbf{M}\cdot\boldsymbol{X}$ is a minimiser of (10). Since the energy $F_{\varepsilon,\text{in-plane}}$ is non-negative, the minimum in the general case, $C \neq 0$ and $\tilde{V}_{\text{WLC}} \neq 0$, is also realised by $\boldsymbol{\chi} = \mathbf{M}\cdot\boldsymbol{X}$, i.e. formula (11) holds.

Case (a)

Set $C \equiv 0$ and let us show that $\boldsymbol{\chi}_{\min} = \mathbf{M}\cdot\boldsymbol{X} + \boldsymbol{u}_{\min}$, with $\boldsymbol{u}_{\min}$ constant, is a solution of the minimisation problem (10)

independent of N. That is, among all $(N-2)$-periodic functions $\boldsymbol{u} \in \mathcal{F}_1(Q_N)$ the energy

$$E_1(\mathbf{M}\cdot\boldsymbol{X}+\boldsymbol{u}, Q_N) \equiv \sum_{\substack{\boldsymbol{X}\in\text{vertexes}\\ \text{in } Q_N}} \frac{1}{2} \sum_{\substack{\boldsymbol{\xi}\in\text{edges in }\Omega\\ \text{connected to } \boldsymbol{X}}} \frac{\sqrt{3}}{2} \tilde{V}_{\text{WLC}}\left(\left(D_1^{\boldsymbol{\xi}}\left(\mathbf{M}\cdot\boldsymbol{X}+\boldsymbol{u}(\boldsymbol{X})\right)\right)^2\right) \tag{12}$$

is minimised by $\boldsymbol{u}_{\min}$ constant. Let us choose an arbitrary minimiser $\tilde{\boldsymbol{u}}_{\min} \in \mathcal{F}_1(Q_N)$ of E_1 given by (12). By definition, the minimiser is at least $N-2$ periodic. Hence, the function $\tilde{\boldsymbol{u}}(\boldsymbol{X}) \in \mathcal{F}_1(Q_N)$ defined by

$$\tilde{\boldsymbol{u}}(\boldsymbol{X}) = \frac{1}{(N-2)^2} \sum_{i,j\in[0,N-2]} \tilde{\boldsymbol{u}}_{\min}(\boldsymbol{X}+i\boldsymbol{g}_1+j\boldsymbol{g}_2)$$

with $\boldsymbol{g}_1$ and $\boldsymbol{g}_2$ defined in (8) is one periodic and thus constant by construction of $\mathcal{F}_1(Q_N)$. By strict convexity of $\tilde{V}_{\text{WLC}}$ and hence strict convexity of E_1, given by (12), the function $\tilde{\boldsymbol{u}}$ satisfies the inequality

$$E_1(\mathbf{M}\cdot\boldsymbol{X}+\tilde{\boldsymbol{u}}, Q_N) < \frac{1}{(N-2)^2} \sum_{i,j\in[0,N-2]} E_1\left(\mathbf{M}\cdot\boldsymbol{X}+\tilde{\boldsymbol{u}}_{\min}\left(\boldsymbol{X}+i\boldsymbol{g}_1+j\boldsymbol{g}_2\right), Q_N\right).$$

Since E_1 depends only on the gradient of $\boldsymbol{\chi}$, it is invariant under a shift, e.g. under the shift $\boldsymbol{X}+i\boldsymbol{g}_1+j\boldsymbol{g}_2$. Hence, we can conclude

$$E_1(\mathbf{M}\cdot\boldsymbol{X}+\tilde{\boldsymbol{u}}, Q_N) < \frac{1}{(N-2)^2} \sum_{i,j\in[0,N-2]} E_1\left(\mathbf{M}\cdot\boldsymbol{X}+\tilde{\boldsymbol{u}}_{\min}\left(\boldsymbol{X}\right), Q_N\right).$$

Therefore also $\tilde{\boldsymbol{u}}(\boldsymbol{X})$ is a minimiser of E_1, and accordingly $\boldsymbol{\chi}_{\min}(\boldsymbol{X}) = \mathbf{M}\cdot\boldsymbol{X}+\tilde{\boldsymbol{u}}(\boldsymbol{X})$. Since $\tilde{\boldsymbol{u}}(\boldsymbol{X})$ is an arbitrary constant and $E_1(\boldsymbol{\chi}, Q_N)$ depends only on the discrete gradient of $\boldsymbol{\chi}$, we can choose $\boldsymbol{\chi}_{\min}(\boldsymbol{X}) = \mathbf{M}\cdot\boldsymbol{X}$. The inequalities are strict, thus uniqueness of the minimiser (up to a constant) is guaranteed.

Case (b)

Choose $\tilde{V}_{\text{WLC}} \equiv 0$ and let us prove that $\boldsymbol{\chi}_{\min} = \mathbf{M}\cdot\boldsymbol{X}$ is also a solution of the minimisation problem (10) for all N. That is, it minimises

$$E_1(\boldsymbol{\chi}, Q_N) \equiv \sum_{\substack{\boldsymbol{X}\in\text{vertexes}\\ \text{in } Q_N}} \frac{1}{3} \sum_{\substack{\boldsymbol{\xi}\in\text{edges in }\\ \text{connected to } \boldsymbol{X}}} \frac{\sqrt{3}}{2} \frac{C}{\left(J_\triangle\left(\boldsymbol{\chi}\left(\boldsymbol{X}\right)\right)\right)^q+\eta} \tag{13}$$

among all $\boldsymbol{\chi} \in \mathcal{F}_{1,\mathbf{M}\cdot\boldsymbol{X}}(Q_N)$.

Let us fix N. For all deformations $\boldsymbol{\chi} \in \mathcal{F}_{1,\mathbf{M}\cdot\boldsymbol{X}}(Q_N)$ the total area of Q_N after the deformation equals $N^2\sqrt{3}/2 \det\mathbf{M}$, since $|Q_N| = N^2\sqrt{3}/2$ and the total area depends only on the value of $\boldsymbol{\chi}$ on ∂Q_N. Hence, it follows

$$N^2\frac{\sqrt{3}}{2}\det\mathbf{M} = \sum_{\substack{\boldsymbol{X}\in\text{vertexes}\\ \text{in } Q_N}} \sum_{\substack{\triangle\in\text{faces in } Q_N\\ \text{connected to } \boldsymbol{X}}} \frac{\sqrt{3}}{4} J_\triangle\left(\boldsymbol{\chi}\left(\boldsymbol{X}\right)\right) \tag{14}$$

for all $\boldsymbol{\chi} \in \mathcal{F}_{1,\mathbf{M}\cdot\boldsymbol{X}}(Q_N)$. Thus energy $E_1(\boldsymbol{\chi}, Q_N)$ given by (13) can be minimised only by a variation of the triangular face areas $\frac{\sqrt{3}}{4} J_\triangle\left(\boldsymbol{\chi}\left(\boldsymbol{X}\right)\right)$ under the constraint that the sum (total area) is constant. Using $J_\triangle\left(\mathbf{M}\cdot\boldsymbol{X}\right) = \det\mathbf{M}$ and (14), we obtain for arbitrary $\boldsymbol{\chi} \in \mathcal{F}_{1,\mathbf{M}\cdot\boldsymbol{X}}(Q_N)$

$$2\sqrt{3}E_1(\mathbf{M}\cdot\boldsymbol{X}, Q_N) = 2N^2\frac{C}{(\det\mathbf{M})^q+\eta} = 2N^2\frac{C}{\left(\frac{1}{2N^2}\sum_{\substack{\boldsymbol{X}\in\text{vertexes}\\ \text{in } Q_N}}\sum_{\substack{\triangle\in\text{faces in}Q_N\\ \text{connected to } \boldsymbol{X}}} J_\triangle\left(\boldsymbol{\chi}\left(\boldsymbol{X}\right)\right)\right)^q+\eta}.$$

By convexity, we have

$$\sum_{\substack{\boldsymbol{X}\in\text{vertexes}\\ \text{in } Q_N}} \sum_{\substack{\triangle\in\text{faces in}Q_N\\ \text{connected to } \boldsymbol{X}}} \frac{C}{\left(J_\triangle\left(\mathbf{M}\cdot\boldsymbol{X}\right)\right)^q+\eta} < \sum_{\substack{\boldsymbol{X}\in\text{vertexes}\\ \text{in } Q_N}} \sum_{\substack{\triangle\in\text{faces in}Q_N\\ \text{connected to } \boldsymbol{X}}} \frac{\sqrt{3}}{2}\frac{C}{\left(J_\triangle\left(\boldsymbol{\chi}\left(\boldsymbol{X}\right)\right)\right)^q+\eta}$$

for any $\boldsymbol{\chi} \in \mathcal{F}_{1,\mathbf{M}\cdot\boldsymbol{X}}(Q_N)$. The energy of the deformation $\boldsymbol{\chi} = \mathbf{M}\cdot\boldsymbol{X}$ is smaller than the energy of any other deformation $\boldsymbol{\chi}$, which shows $\boldsymbol{\chi}_{\min} = \mathbf{M}\cdot\boldsymbol{X}$ and thus completes the proof. Strict convexity implies the uniqueness of the minimiser. □

So far we have restricted us to 2D deformations on a bounded 2D domain. In the fully 3D situation, i.e.

$$\boldsymbol{\chi} \in W^{1,p}(\Gamma_X;\mathbb{R}^3) \quad \text{with } \det\nabla_X\boldsymbol{\chi} > 0$$

with Γ_X being the surface of the RBC in the undeformed state, i.e. reference configuration, we find

$$F_{\text{in-plane}}(\boldsymbol{\chi}) = \int_{\Gamma_X} \frac{1}{2}\sum_{i=1,\dots,6} \tilde{V}_{\text{WLC}}(\boldsymbol{\xi}^T\cdot{\mathbf{F}^\Gamma}^T\cdot\mathbf{F}^\Gamma\cdot\boldsymbol{\xi}) + 2\frac{C}{(J^{\Gamma q}+\eta)}\mathrm{d}\mu, \tag{15}$$

where $\mathbf{F}^\Gamma \equiv (\nabla_X\boldsymbol{\chi})\cdot\mathbf{P}_X = \mathbf{P}\cdot(\nabla_X\boldsymbol{\chi})\cdot\mathbf{P}_X \in R^{3\times3}$ is the 3D surface deformation tensor, $\mathbf{P}_X = \boldsymbol{n}_X\otimes\boldsymbol{n}_X$ the surface projection operator with respect to the reference configuration (indicated by the subscript X), $\mathbf{P} = \boldsymbol{n}\otimes\boldsymbol{n}$ the one with respect to the current configuration ($\boldsymbol{n}_X$ and $\boldsymbol{n}$ are outer unit normals of the surface), and the surface Jacobian J^Γ. The latter is given by $J^\Gamma = \sqrt{\det\mathbf{g}}$ with the metric tensor g of the surface, defined as

$$(\mathbf{g})_{ij} = (\mathbf{F}^\Gamma\cdot\boldsymbol{t}_i)^T\cdot(\mathbf{F}^\Gamma\cdot\boldsymbol{t}_j) \qquad \text{with } i,j\in\{1,2\}$$

where $\boldsymbol{t}_1$ and $\boldsymbol{t}_2$ are two orthogonal vectors in the tangent space of the surface.

3.4 Characterisation of $F_{\text{in-plane}}$ using invariants of $\mathbf{F}^\Gamma$

For simplicity, let us first restrict to Taylor expansions $\tilde{V}_{\text{WLC}}$ of V_{WLC} around 1 up to order 2, i.e. $p = 2$. We thus find the following energy density Ψ:

$$\Psi = \frac{1}{2}\sum_{i=1,\dots,6}\Big(V_{\text{WLC}}(1) + V'_{\text{WLC}}(1) \times (\boldsymbol{\xi}^T \cdot \boldsymbol{F}^{\Gamma T} \cdot \boldsymbol{F}^\Gamma \cdot \boldsymbol{\xi} - 1) + \frac{1}{2}V''_{\text{WLC}}(1)(\boldsymbol{\xi}^T \cdot \boldsymbol{F}^{\Gamma T} \cdot \boldsymbol{F}^\Gamma \cdot \boldsymbol{\xi} - 1)^2\Big) + 2\frac{C}{J^{\Gamma q} + \eta} \tag{16}$$

with V_{WLC} defined in (5).

The energy (16) is isotropic, which is a well-known result. (In the general case $p > 2$ the energy density (15) is not isotropic and has a hexagonal symmetry!) This allows us to rewrite the energy density in terms of invariants of the deformation tensor, a standard approach in non-linear elasticity. Throughout the literature different invariants are used in the context of hyperelastic materials. Here, we work with the following invariants (Skalak et al. 1973):

$$\begin{aligned} I_1 &\equiv J^\Gamma - 1 = \lambda_1\lambda_2 - 1, \\ I_2 &\equiv \operatorname{tr}(\mathbf{F}^\Gamma \cdot (\mathbf{F}^\Gamma)^{\mathrm{T}}) - 2 = \lambda_1^2 + \lambda_2^2 - 2, \end{aligned} \tag{17}$$

where λ_1 and λ_2 are the principal stretches of the surface deformation tensor $\mathbf{F}^\Gamma$: Using the relation between interaction link lengths and invariants (c.f Appendix) as well as dropping constant terms, we find:

$$\Psi = \frac{3}{2}V'_{\text{WLC}}(1)I_2 + \frac{3}{16}V''_{\text{WLC}}(1)(4I_2 - 8I_1 + 3I_2^2 - 4I_1^2) + 2\frac{C}{(I_1^q + \eta)}.$$

For the rest of this section let us assume that the membrane skeleton is initially not stressed. This assumption might not hold true in all cases. Pre-stress is an important concept in biology (Boey et al. 1998; Ingber 2003). However, our assumptions allow us the explicit specification of the constant C. Considering deformations consisting only of compression, or alternatively dilatation, i.e. $I_2 = 2I_1$, we obtain the following expansion

$$\Psi = 2C + (3V'_{\text{WLC}}(1) - \frac{2Cq}{(1+\eta)^2})I_1 + \mathcal{O}(I_1^2).$$

Assuming that the network is initially unstressed, the energy should be at a minimum and hence all linear terms should vanish. We therefore find

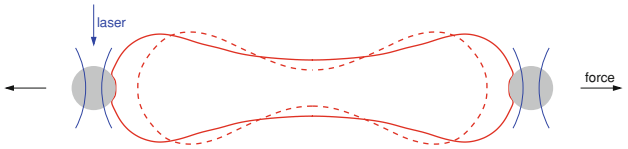

Fig. 3 Illustration of a typical optical tweezers experiment

$$C = \frac{3(1+\eta)^2 V'_{\text{WLC}}(1)}{2q}$$

and thus are left with one constant less, allowing a better comparison with experiments. A direct relation of the microscopic parameters with macroscopic moduli is possible and is considered in Sect. 4.3.

Of course the same approach can be applied in the case $p > 2$. For $p > 2$, however, the hexagonal symmetry is reflected in (16). Whether a stress tensor with a hexagonal symmetry is biologically realistic or not is unclear. On one hand it is not clear in which direction the symmetry axis would be pointing, on the other hand the spectrin network is not perfectly symmetric, it only shows largely a hexagonal symmetry (over 80% degree-6 vertexes). Further, it is not clear how a hexagonal symmetry could be identified from an experimental point of view. For simplicity, we average over all possible directions of symmetry axis in the case $p > 2$: $\bar{\Psi} = \int_0^{2\pi} \Psi \mathrm{d}\phi$, c.f. Appendix. The assumption of a hexagonal symmetry is, however, necessary for the sake of the derivation of a homogenisation formula. Only this homogenisation formula allows the direct linkage between microscopic and macroscopic models and corresponding parameters.

4 A relaxation approach

The models considered above are based on a static description in terms of energy functionals, i.e. shapes of RBCs are determined by energy minimisation. The corresponding energy minima are typically calculated using the corresponding Euler–Lagrange equations (Dacorogna 2004). Physically speaking, the corresponding forces of the energies are determined and one looks for a shape where all forces equilibrate.

Instead of using the Euler–Lagrange equations, we consider a relaxation approach based on a dynamic formulation in the framework of conservation of mass and linear momentum for the simulation of optical tweezers experiments (illustrated in Fig. 3). Such an approach is of course somewhat more complex, but has several advantages. On one hand it can be easily extended to situations, where dynamics play a role, as well as it can be easily compared with existing dynamic models (Pozrikidis 2003a,b). On the other hand it can be encoded directly in the FEM-framework GASCOIGNE (Becker et al. 2009).

We adopt the same assumption as in Sect. 1.2: the time scale of the experiment (order of seconds) is fast compared to relaxation (at least order of several minutes), thus that we consider the regime of membrane elasticity. Additionally, we assume that the cytosol is locally incompressible as well as a globally constant surface area, rather than choosing very large k_{volume} and k_{volume} in Model 1. Moreover, we neglect inertial effects of the membrane, since its mass is relatively small.

Model 2 The mechanics of a RBC clamped into an optical tweezers (schematically shown in Fig. 3) are determined by the following model (for some fixed time $T > 0$):

$$\begin{aligned}
\frac{\mathrm{d}\boldsymbol{u}}{\mathrm{d}t} &= \boldsymbol{v} && \text{in } \Omega_{\text{cell}}(t)\times[0,T),\\
\rho\frac{\mathrm{d}\boldsymbol{v}}{\mathrm{d}t} &= -\nabla p + \nabla\cdot\boldsymbol{\sigma}_{\text{cytosol}} && \text{in } \Omega_{\text{cell}}(t)\times[0,T),\\
0 &= \nabla\cdot\boldsymbol{v} && \text{in } \Omega_{\text{cell}}(t)\times[0,T),\\
&(\boldsymbol{\sigma}_{\text{cytosol}} + p_{\text{out}}\mathbf{1})\cdot\boldsymbol{n} && \text{on } \partial\Omega_{\text{cell}}(t)\times[0,T),\\
&= \boldsymbol{F}_{\text{tweezers}} - \nabla^{\Gamma} q_{\text{surf.}} + \boldsymbol{F}_{\text{membrane}}\\
&|\partial\Omega_{\text{cell}}(t)| = |\partial\Omega_{\text{cell}}(0)| && \text{for } [0,T).
\end{aligned}$$

The evolution of $\Omega_{\text{cell}}(t)$ is given by the speed $\boldsymbol{v}$ on the boundary.

As usual ρ is the local material density, $\boldsymbol{v}$ the local material speed, $\boldsymbol{u}$ is the local material displacement, i.e. the current position of a particle originating position $\boldsymbol{X}$ in the reference configuration is given by $\boldsymbol{x} = \boldsymbol{X} + \boldsymbol{u}(\boldsymbol{X})$ and p is the local volume pressure, accounting for incompressibility of the cytosol. The global surface pressure $q_{\text{surf.}}$ is constant on the surface since the single constraint $|\partial\Omega_{\text{cell}}(t)| = |\partial\Omega_{\text{cell}}(0)|$ requires only one Lagrange multiplier. $\nabla = \nabla_x$ is the gradient with respect to the laboratory coordinate system and $\nabla^{\Gamma} = \mathbf{P}\cdot\nabla$ is the surface gradient, where $\mathbf{P}$ is the surface projection operator. Here, we have assumed that σ_{cytosol} is given by the Stokes stress tensor, i.e.

$$\boldsymbol{\sigma}_{\text{cytosol}} = \eta\left(\nabla\boldsymbol{v} + (\nabla\boldsymbol{v})^{T}\right),$$

and $\boldsymbol{F}_{\text{tweezers}}$ is the force density due to the optical tweezers, i.e.

$$\boldsymbol{F}_{\text{tweezers}} = \chi_{\text{tweezers}}\boldsymbol{f}_{\text{tweezers}}$$

with the characteristic function of the microbeads χ_{tweezers} and the constant force density due to optical tweezers f_{tweezers}. The boundary force density $\boldsymbol{F}_{\text{membrane}}$ describes the resistance to stretching and bending of the membrane and will be discussed in detail below. Relation $\nabla\cdot\boldsymbol{v} = 0$ in $\Omega_{\text{cell}}(t)\times[0,T)$ ensures incompressibility of the volume (cytosol) and $|\partial\Omega_{\text{cell}}(t)| = |\partial\Omega_{\text{cell}}(0)|$ ensures incompressibility of the membrane.

So far we have not specified the force density $\boldsymbol{F}_{\text{membrane}}$ due to surface mechanics. Using a variational approach we can relate the energies derived in Sect. 3 with corresponding forces, i.e. forces are given by the steepest decent of the L^2-gradient of the free energy. Since this approach corresponds to the derivation of the Euler–Lagrange equations, stationary states of Model 2 are minimisers of the continuum version of Model 1, as derived in Sect. 3.

Considering static microscopic (Sect. 2) and macroscopic (Sect. 3) descriptions of RBCs in terms of energy functionals, the energies corresponding to bending and in-plane mechanics are not coupled. Therefore, also the corresponding forces are not coupled and we can split up $\boldsymbol{F}_{\text{membrane}}$ into two terms:

$$\boldsymbol{F}_{\text{membrane}} = \boldsymbol{T} + \boldsymbol{N},$$

where $\boldsymbol{N}$ is the force due to resistance to bending, and $\boldsymbol{T}$ the force due to in-plane stresses. Both membrane forces $\boldsymbol{N}$ and $\boldsymbol{T}$ are determined by the steepest decent of the L^2- gradient of the corresponding membrane energies.

4.1 Resistance to in-plane deformations: T

The energy corresponding to the resistance to in-plane deformations is given by (15) with the initial shape Γ_X of the membrane. Let us consider small variations $\boldsymbol{X}_{\varepsilon} = \boldsymbol{X} + \varepsilon\boldsymbol{\phi}$, where $\boldsymbol{\phi}$ is an arbitrary test function which is infinitely often differentiable, i.e. $\boldsymbol{\phi}\in C^{\infty}(\Gamma;\mathbb{R}^3)$. Using Jacobi's formula, i.e. $\frac{\partial}{\partial\varepsilon}J^{\Gamma} = J^{\Gamma}\mathrm{tr}((\mathbf{F}^{\Gamma})^{-1}\cdot\frac{\partial}{\partial\varepsilon}\mathbf{F}^{\Gamma})$ and $\frac{d}{d\varepsilon}\mathbf{F}^{\Gamma}|_{\varepsilon=0} = \nabla_X^{\Gamma}\boldsymbol{\phi} = \left(\nabla^{\Gamma}\boldsymbol{\phi}\right)\cdot\mathbf{F}^{\Gamma}$, we find

$$\begin{aligned}
\frac{\mathrm{d}}{\mathrm{d}\varepsilon}F_{\text{in-plane}}\bigg|_{\varepsilon=0} = \int_{\Gamma_X}\Bigg[&\frac{1}{2}\sum_{i=1,\dots,6}\tilde{V}'_{\text{WLC}}(|\boldsymbol{\xi}_1|^2)\hat{\boldsymbol{\xi}}_i\cdot\left((\nabla^{\Gamma}\boldsymbol{\phi})\right.\\
&\left.+(\nabla^{\Gamma}\boldsymbol{\phi})^{T}\right)\cdot\hat{\boldsymbol{\xi}}_i - \frac{2Cq\,J^{\Gamma q-1}}{(J^{\Gamma q}+\eta)^2}J^{\Gamma}\mathrm{tr}(\nabla^{\Gamma}\boldsymbol{\phi})\Bigg]\mathrm{d}\mu_X,
\end{aligned}$$

where $\hat{\boldsymbol{\xi}}_i = \mathbf{F}^{\Gamma}\cdot\boldsymbol{\xi}_i$ is the vector of the ith link after the deformation $\mathbf{F}^{\Gamma}$. Using $\int_{\Gamma}\boldsymbol{T}\cdot\boldsymbol{\phi}\mathrm{d}\mu = \left\langle F'_{\text{in-plane}},\boldsymbol{\phi}\right\rangle = \frac{\mathrm{d}}{\mathrm{d}\varepsilon}F_{\text{in-plane}}|_{\varepsilon=0}$ with force density $\boldsymbol{T}$ yields after integration by parts:

$$\boldsymbol{T} = \nabla^{\Gamma}\cdot\boldsymbol{\tau}$$

with the so-called surface stress tensor

$$\boldsymbol{\tau} = \frac{1}{2J^{\Gamma}}\sum_{i=1,\dots,6}\frac{1}{\mathcal{L}_i}\frac{\partial\tilde{V}_{\text{WLC}}(\mathcal{L}_i)}{\partial\mathcal{L}_i}\hat{\boldsymbol{\xi}}_i\otimes\hat{\boldsymbol{\xi}}_i - 2q\frac{C}{J^{\Gamma q+1}}\mathbf{1}. \quad (18)$$

Boundary terms do not need to be considered since Γ_X, and accordingly Γ, is a closed surface.

The stress tensor $\boldsymbol{\tau}$ defined above generally reflects the hexagonal symmetry of the underlying network. Considering the case $p = 2$ or working with averaged energies $\bar{F} = \int_0^{2\pi}F\mathrm{d}\phi$ with respect to the symmetry axis (c.f. Sect. 3.4) the considered energies are isotropic and thus can be characterised by the invariants of the surface deformation tensor $\mathbf{F}^{\Gamma}$ alone. The variational approach yields

$$\boldsymbol{\tau} = \frac{2}{1+I_1}\frac{\partial\Psi(I_1,I_2)}{\partial I_2}\boldsymbol{F}^{\Gamma}\cdot\boldsymbol{F}^{\Gamma T} + \frac{\partial\Psi(I_1,I_2)}{\partial I_1}\mathbf{P}.$$

A direct relation of macroscopic moduli with microscopic moduli is given further below in Sect. 4.3.

4.2 Resistance to bending: $\boldsymbol{N}$

Normal forces $\boldsymbol{N}$ are uniquely due to the resistance of the membrane to bending. Let the bending energy of the membrane be given by the Canham–Helfrich energy. In the following, we consider small variations $\boldsymbol{X}_\varepsilon = \boldsymbol{X} + \varepsilon \boldsymbol{n}\phi$, where $\boldsymbol{n}$ is the outer unit normal of the surface Γ and $\phi \in C^\infty(\Gamma;\mathbb{R})$ is an arbitrary test function. It is sufficient to consider only variations $\varepsilon \boldsymbol{n}\phi$, since a variation in the normal direction completely describes the evolution of the interface.

Following Willmore (1993) (Attention, Willmore uses a different definition of mean curvature, i.e. $H_{\text{Willmore}} = -H/2$), the variation of the mean curvature is given by

$$\begin{aligned}\frac{\mathrm{d}}{\mathrm{d}\varepsilon} H_\varepsilon \Big|_{\varepsilon=0} &= -\Delta^\Gamma \phi - \phi |\nabla^\Gamma \boldsymbol{n}|^2 \\ &= -\Delta^\Gamma \phi - \phi (H^2 - 2K)\end{aligned}$$

and the variation of the integration measure is given by

$$\frac{\mathrm{d}}{\mathrm{d}\varepsilon} \mathrm{d}\mu_\varepsilon \Big|_{\varepsilon=0} = \phi H \mathrm{d}\mu.$$

Here, Δ^Γ is the Laplace–Beltrami operator (surface Laplace). Hence, we find

$$\begin{aligned}&\frac{\mathrm{d}}{\mathrm{d}\varepsilon} \frac{\kappa}{2} \int_{\Gamma_\varepsilon} (H_\varepsilon - H_0)^2 \mathrm{d}\mu_\varepsilon \Big|_{\varepsilon=0} \\ &\quad = -\frac{\kappa}{2} \int_\Gamma [2(H - H_0)(\Delta^\Gamma \phi + \phi(H^2 - 2K)) \\ &\qquad - (H - H_0)^2 \phi H] \mathrm{d}\mu.\end{aligned}$$

Under the assumption that $\boldsymbol{N}$ is determined by the steepest decent of $F_{\text{Canham–Helfrich}}$, defined in (7), i.e. $\int_\Gamma \boldsymbol{N} \cdot (\boldsymbol{n}\phi) \mathrm{d}\mu = -\left\langle F'_{\text{bending}}, \phi \right\rangle = -\frac{d}{d\varepsilon} \frac{\kappa}{2} \int_{\Gamma_\varepsilon} (H_\varepsilon - H_0)^2 \mathrm{d}\mu_\varepsilon |_{\varepsilon=0}$, we find

$$\boldsymbol{N} = \kappa \left(\Delta^\Gamma H + (H - H_0)(H^2 - 2K) - \frac{1}{2}(H - H_0)^2 H \right) \boldsymbol{n},$$

where we have used the product rule and Green's theorem for surfaces. Setting the material speed $\boldsymbol{v}$ proportional to $\boldsymbol{N}$ and considering the case $H_0 = 0$, the so-called Willmore flow is obtained (Willmore 1993).

4.3 Linear elasticity

The mechanical properties of the membrane within the continuum mechanical Model 2 are determined by the underlying continuum energies, which are directly related to the properties the discrete network. Thus we can relate the modulus of rigidity μ and modulus hydrostatic compression K, used in linear elasticity, directly with the properties of the discrete atomistic model. Considering small deformations and restricting ourselves to linear elasticity, i.e. performing a Taylor extension considering only linear terms, we recover from (18)

$$\begin{aligned}\mu &= 3V'_{\text{WLC}}(1) + \frac{3}{2} V''_{\text{WLC}}(1), \\ K &= \frac{3(1 + \eta + q - q\eta)}{1 + \eta} V'_{\text{WLC}}(1) + 3V''_{\text{WLC}}(1),\end{aligned}$$

respectively

$$\begin{aligned}\mu &= \frac{\sqrt{3} k_B T (-16L^3 + 51L^2 \mathcal{L}_{\max} - 57L\mathcal{L}_{\max}^2 + 24\mathcal{L}_{\max}^3)}{16(p\mathcal{L}_{\max}(-L + \mathcal{L}_{\max})^3}, \\ K &= \frac{3(1 + \eta + q - q\eta)}{1 + \eta} \frac{\sqrt{3} k_B T (4L^2 - 9L\mathcal{L}_{\max} + 6\mathcal{L}_{\max}^2}{12p\mathcal{L}_{\max}(-L + \mathcal{L}_{\max})^2} \\ &\quad + \frac{\sqrt{3} k_B T L(-L + 3\mathcal{L}_{\max})}{8p(-L + \mathcal{L}_{\max})^3}.\end{aligned}$$

Table 1 Parameters proposed of the worm-like chain model V_{WLC} (Li et al. 2005)

$L = 75.00\,\text{nm}$	$\mathcal{L}_{\max} = 237.75\,\text{nm}$
$p = 7.50\,\text{nm}$	$T = 300.00\,\text{K}$

Postulated parameters of Li et al. (2005) for the worm-like chain model V_{WLC} are summarised in Table 1. Using further $k_B = 1.38 \times 10^{-23}\,\frac{\text{J}}{\text{K}}$, choosing $q = 1$ and $\eta = 0.005$, we find

$$\begin{aligned}\mu &= 8.3 \times 10^{-6}\,\frac{\text{N}}{\text{m}}, \\ K &= 16.6 \times 10^{-6}\,\frac{\text{N}}{\text{m}},\end{aligned}$$

which agrees with experimental results (Mohandas and Evans 1994; Lenormand et al. 2001).

5 Simulations

In Model 2, the bulk mechanics are given by the incompressible Navier–Stokes equation. These are second-order equations which are quite well studied from an analytical as well as numerical point of view. The tangential component of the surface mechanics is a typical example of a hyperelastic material. It is also a second-order equation. On the other hand, the normal mechanics of the lipid bilayer involve fourth-order derivatives and the structure is nearly identical to the so-called Willmore flow as discussed above. The coupling of the different models, especially the coupling of surface (2D models on a hypersurface) with bulk mechanics (3D models), makes analytical and computational investigations of Model 2 quite challenging. Here, we restrict ourselves to an investigation of the fluid(3D)-structure(2D)-interaction from a numerical point of view.

Since we are only interested in stationary shapes, we simplify Model 2 further by considering stationary Stokes flow instead of the full Navier–Stokes equations. However, an approach considering the full Navier–Stokes equations is as well as feasible. We would like to work with a discretisation via the standard Galerkin procedure, i.e. using the same type of ansatz functions for all variables. Thus we need to consider a stabilised Stokes approach guaranteeing the Babuska–Brezzi condition (Rannacher 2006):

$$\begin{aligned} 0 &= \nabla \cdot \boldsymbol{\sigma}_{\text{cytosol}} && \text{in } \Omega_{\text{cell}}(t) \times [0,T), \\ 0 &= \nabla \cdot (\boldsymbol{v} + \varepsilon_{\text{stab},1} \nabla p) && \text{in } \Omega_{\text{cell}}(t) \times [0,T) \end{aligned} \tag{19}$$

with an additional natural boundary condition for p, i.e.

$$\boldsymbol{n} \cdot \nabla p = 0 \quad \text{on } \partial\Omega_{\text{cell}}(t) \times [0,T),$$

where $\varepsilon_{\text{stab},1}$ is the stabilisation parameter (typically $\varepsilon_{\text{stab},1} \approx \frac{\delta x^2}{\eta}$ with spatial discretisation size δ_x). Generally, the solutions depend only weakly on the exact value of $\varepsilon_{\text{stab},1}$. The global pressure $q_{\text{surf.}}$ is realised via the Chorin–Uzawa scheme (Rannacher 2006), i.e. through the introduction of artificial compressibility:

$$\varepsilon_{\text{stab},2} \frac{\mathrm{d}q_{\text{surf}}}{\mathrm{d}t} = |\partial\Omega_{\text{cell}}(0)| - |\partial\Omega_{\text{cell}}(t)| \quad \text{for } [0,T), \tag{20}$$

where $\varepsilon_{\text{stab},2}$ is again a small constant.

5.1 Weak formulation and discretisation

With respect to the finite element method, appropriate weak formulations need to be derived. Apart from the bending forces $\boldsymbol{N}$ of the membrane mechanics the derivation is straightforward. A derivation of an appropriate weak formulation for the Willmore flow can be found in Rusu (2005). Slight modifications of the approach yield a weak formulation of the membrane mechanics considered here (Hartmann 2007).

The weak formulation of model (2) with stabilisations (19) and (20) is given by:

$$\int_{\Omega(t)} \phi \frac{\mathrm{d}\boldsymbol{u}}{\mathrm{d}t} \mathrm{d}\mu = \int_{\Omega(t)} \phi \boldsymbol{v} \mathrm{d}\mu,$$

$$0 = \int_{\Omega(t)} \boldsymbol{\sigma}_{\text{cytosol}} \cdot \nabla\phi \mathrm{d}\mu,$$

$$0 = \int_{\Omega(t)} \phi \nabla \cdot \boldsymbol{v} - \varepsilon_{\text{stab},1} \nabla p \cdot \nabla\phi \mathrm{d}\mu,$$

and

$$\begin{aligned} \int_{\partial\Omega(t)} \phi^\Gamma (\boldsymbol{\sigma}_{\text{cytosol}} + p_{\text{out}}\mathbf{1}) \cdot \boldsymbol{n} \mathrm{d}\mu &= - \int_{\partial\Omega(t)} \boldsymbol{\tau} \cdot (\nabla^\Gamma \phi^\Gamma) \mathrm{d}\mu \\ &- \kappa \int_{\partial\Omega(t)} \frac{1}{2} |\boldsymbol{Y}|^2 (\nabla^\Gamma \boldsymbol{x}) \cdot (\nabla^\Gamma \phi^\Gamma) - (\nabla^\Gamma \boldsymbol{Y}) \cdot (\nabla^\Gamma \phi^\Gamma) \\ &+ 2\boldsymbol{n} \otimes \boldsymbol{n} \cdot (\nabla^\Gamma \boldsymbol{Y}) \cdot (\nabla^\Gamma \phi^\Gamma) \mathrm{d}\mu + \int_{\partial\Omega(t)} \phi^\Gamma \boldsymbol{F}_{\text{tweezers}} \mathrm{d}\mu, \end{aligned}$$

$$\varepsilon_{\text{stab},2} \frac{\mathrm{d}q_{\text{surf}}}{\mathrm{d}t} = |\partial\Omega_{\text{cell}}(0)| - |\partial\Omega_{\text{cell}}(t)|,$$

$$\int_{\partial\Omega(t)} \phi^\Gamma \boldsymbol{Y} \mathrm{d}\mu = \int_{\partial\Omega(t)} (\nabla^\Gamma \boldsymbol{x}) \cdot (\nabla^\Gamma \phi^\Gamma) - \phi H_0 \boldsymbol{n} \mathrm{d}\mu,$$

where $\phi \in C_0^\infty(\Omega(t); \mathbb{R})$ and $\phi^\Gamma \in C^\infty(\partial\Omega(t); \mathbb{R})$ are arbitrary test functions.

The strong and weak formulations of the surface evolution given above are all based on the Eulerian description. A Lagrangian description is, however, more appropriate with respect to an implementation using standard finite element packages. The weak formulation of Model 2 given above has been transformed accordingly to a Lagrangian (fixed) coordinate system (for more details see Hartmann (2007)) and implemented using the finite element library GASCOIGNE (Becker et al. 2009).

The software package GASCOIGNE does not allow the differentiation between surface and bulk variables using one implicitly time-stepping scheme for membrane and bulk processes. (Since membrane mechanics involve spatial derivatives of fourth order, explicit time-stepping schemes would imply very small time steps; Clarenz et al. 2004). Hence, variables defined only on the boundary have to be extended appropriately. Here, we have chosen an extension by Laplace's equation. The surface speed $\boldsymbol{v}^\Gamma$ and the bulk speed $\boldsymbol{v}$ are considered as one variable, which allows a direct implicit coupling. Since the weak formulation of Model 2 involves only first-order derivatives, we use tri-linear finite elements in the bulk part and accordingly bi-linear finite elements on the surface. The evolution in time is discretised with a fractional-theta scheme. Using Newton's method, the resulting non-linear systems are solved. Corresponding linearisations are solved with a GMRES preconditioner and a multigrid method. The scheme has been thoroughly tested and shows a reasonable order of convergence larger than 1.5, which is in good agreement with the results for Willmore flows reported by Clarenz et al. (2004).

Taking advantage of reflection symmetries with respect to the coordinate planes, we can reduce the computational effort by considering only one-eighth of the object. Moreover, the finite element toolkit GASCOIGNE offers the possibility of local mesh refinement, which allows a further reduction of

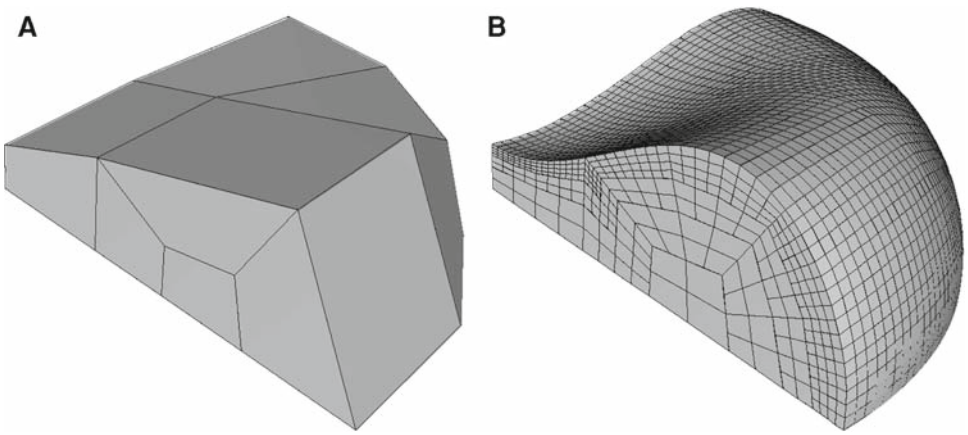

Fig. 4 Typical discretisations: **a** initial discretisation; **b** discretisation after grid refinement (2,048 surface quadrilaterals)

computational effort. Since the dynamics of Model 2 are driven by membrane mechanics, we have chosen an adaptive discretisation refined in the vicinity of the surface (see Fig. 4).

5.2 Initial shapes of RBCs

A quantitative characterisation of the rest shape of RBCs has been given by Evans and Skalak (1980), c.f. formula (1), and could be used as an initial condition. On the other hand it has been postulated by Li et al. (2005) that the rest shape is an energy minimiser of the Canham–Helfrich energy $F_{\text{Canham–Helfrich}}$.

Independent of the chosen initial shape we follow (Li et al. 2005) and assume that the attachment of the microbead to the RBC does not alter the initial shape of the RBC. This is of course a quite crude assumption, but it should not influence the results quantitatively on the order of experimental accuracy. Let the contact area of the microbead with respect to the reference configuration be given by

$$\partial\Omega_{\text{tweezers},0} = \{\boldsymbol{x} = (x, y, z) \in \partial\Omega_{\text{cell},0} : x^2 + z^2 \leq R^2_{\text{tweezers}}\},$$

where $R_{\text{tweezers}} = 1.3\,\mu\text{m}$. This corresponds to an area of contact of approximately $6.7\,\mu\text{m}^2$ per bead, i.e. the force due to the two optical tweezers is applied to 10% of the surface area as proposed by Li et al. (2005).

5.3 Simulation results

Here we use the same parameters of the microscopic model as Li et al. (2005), summarised in Table 1, to which we would like to compare our continuum approach. Other parameters of Model 2 according to the literature are summarised in Table 2. The spontaneous membrane curvature can be "guessed" only roughly: According to Evans and Skalak (1980) the volume of the RBC equals $V = 1.57 R_0^3 = 94.10\,\mu\text{m}^3$, which corresponds to a ball of radius $R = 2.82\,\mu\text{m}$. We therefore expect the spontaneous membrane curvature in the range from $H_0 = 0$ to $H_0 = \frac{1}{2.82} \times 10^6\,\text{m}^{-1}$.

5.3.1 Relaxation experiments

Li et al. (2005) have proposed that rest shapes of RBCs minimise the Canham–Helfrich energy (7), since the membrane-bound cytoskeleton is constantly rearranging and thus allows relaxation of any stresses on long time scales. The minimal energy configuration of the Canham–Helfrich energy depends solely on the volume/area ratio and the spontaneous curvature H_0 (Seifert et al. 1991). The rest shape given by formula (1) is based on an experimental characterisation of RBCs by Evans and Skalak (1980). Hence, it might not necessarily be a minimal energy configuration with respect to the Canham–Helfrich energy.

Let us neglect the mechanics of the membrane-associated cytoskeleton for the moment. Simulations with an initial shape given by formula (1) with $R = 3.91\,\mu\text{m}$ are shown in Fig. 5. The shape has been allowed to relax over 3 s (10^4 time steps), after which the velocity is virtually zero. Since the shape has relaxed only slightly, we can conclude that the minimal energy configuration of the Canham–Helfrich energy with $H_0 = 0.1 \times 10^{-6}\,\text{m}^{-1}$ is indeed close to the experimentally observed rest shapes. A variation of H_0 within the range $0–0.2 \times 10^{-6}\,\text{m}^{-1}$ does not change the results qualitatively.

Table 2 Experimentally determined parameters

Bending elasticity κ	$2 \times 10^{-19}\,\text{J}$	see Scheffer et al. (2001) and Mohandas and Evans (1994)
Cytosol viscosity η	$6.0\text{cp} = 6.0 \times 10^{-3}\,\text{Pa s}$	see Pozrikidis (2003a)
Spont. membrane curvature H_0	$0 - 0.35 \times 10^6\,\text{m}^{-1}$	see text

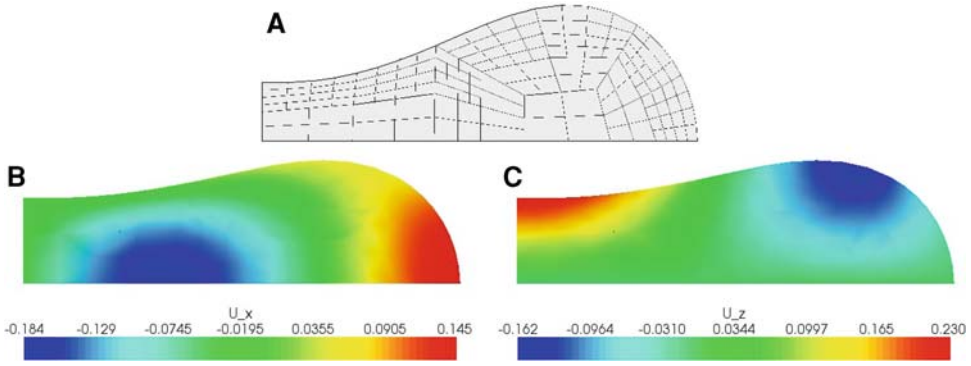

Fig. 5 Relaxation of the initial shape of a red blood cell given by Evans and Skalak (1980), i.e. formula (1), with $R = 3.91$ µm. Here, we have used an implicit Euler time stepping scheme with time step size $\delta t = 0.0003$ s and parameters given in Table 2. **a** Shows the initial shape given by formula (1). **b, c** Show the relaxed shape after 3 s. In **b** the deformation in the radial direction and in **c** the deformation in the z-direction is shown

5.3.2 Force experiments

Typical experiments consider microbeads subject to a constant force. The objective of such force experiments is to measure the longitudinal and transversal radii as a function of the applied stretching force (Hénon et al. 1999; Li et al. 2005). Here, we consider the same experiments in silico using Model 2 with the initial shape determined above (Sect. 5.3.1). The evolution of a RBC subject to a constant force applied via optical tweezers is shown in Fig. 6. After some time the RBC converges to a fixed shape. The elastic energy stored in the membrane is relaxed and has reached an energy minimum. The relaxed shape agrees qualitatively with the discrete model of Li et al. (2005) as well as with the shapes observed by Hénon et al. (1999).

The relation between applied forces and axial as well as transversal diameters obtained from several simulations (Fig. 7) agrees within experimental accuracies quantitatively well with experimental results reported in the literature (Hénon et al. 1999; Li et al. 2005). Especially, considering experiments up to forces of 200 pN Model 2 based on a Taylor expansion of the potential V_{WLC} up to second order, i.e. $p = 2$, approximates the proposed microscopic model (Li et al. 2005) extremely well (with significantly less computational

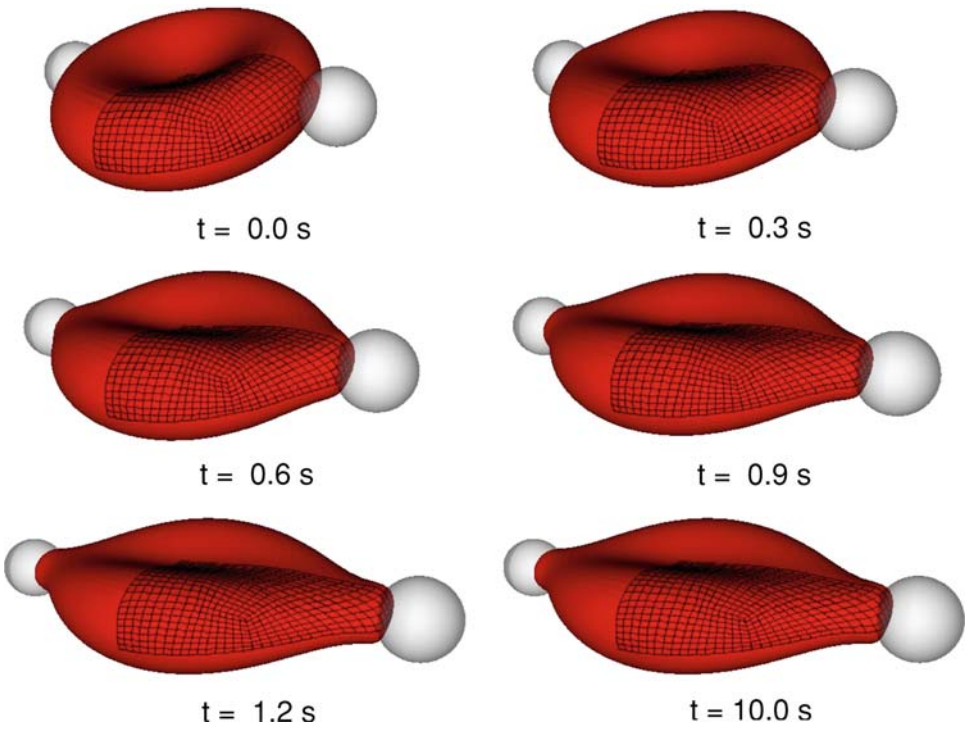

Fig. 6 Evolution of a red blood cell (Model 2). Parameters of the model are summarised in Tables 1 and 2. The results have been obtained using an implicit Euler scheme with time step size $\delta t = 1.0 \times 10^{-3}$ s

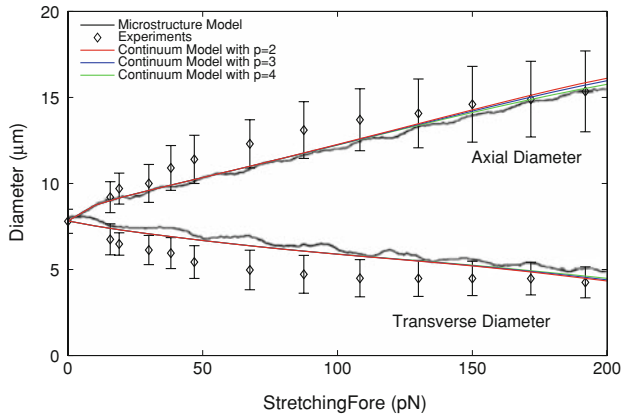

Fig. 7 Diameters of stretched red blood cell for different prescribed forces, which have been determined using finite element simulations of Model 2. Parameters of the model are summarised in Tables 1 and 2. Here we have used an implicit Euler scheme with time step size $\delta t = 0.06$ s. For $p > 2$, the Model 2 is based on the averaging scheme outlined in Appendix, i.e. the membrane is isotropic. The results are compared with experimental results and simulations of the microscopic model according to Li et al. (2005) (©2005 Biophysical Society)

effort). Only for forces larger than 200 pN the full non-linear model would be necessary.

6 Discussion

In this article we have shown how concepts from Γ-convergence, introduced for the derivation of continuum macroscopic models from atomistic interactions in crystal lattices (Alicandro and Cicalese 2004), can be generalised to biomechanical problems. As a test case we have considered RBCs. From a well-studied discrete microscopic model in terms of energy functionals we have first derived a corresponding continuum energy functional for the membrane-bound cytoskeleton. Corresponding energy minimising shapes (observed shapes) have been determined using a relaxation approach. At the same time, an easily extendable continuum mechanical model for RBCs has been derived.

Our multiscale model considers the membrane as a 2D hypersurface, whose mechanical properties are determined by the lipid bilayer and the membrane-bound spectrin network. The latter explicitly includes molecular details inherited by multiscale analysis. Only very few models consider the mechanics of RBCs in a similar realistic setting. Often the membrane is assumed to be a 3D solid with small but finite thickness (Dao et al. 2003; Mills et al. 2004) or the bending-resistance of the lipid bilayer is given by quite heuristic models (Pozrikidis 2003a). The multiscale nature of the continuum model derived in this work allows to benefit from advantages of continuum models like efficient numerical schemes based on adaptive discretisation techniques (the discretisation can be chosen independent of the microscopic geometry) without neglecting important microscopic details. All microscopic parameters can be directly related to macroscopic parameters in a quantitative way.

Our approach required the assumption of a hexagonal symmetry for the sake of a homogenisation formula. This implies that in the general case the hexagonal symmetry is reflected in the continuum mechanical equations, which might not be realistic from a biological point of view. The spectrin network shows only roughly hexagonal symmetry (over 80% degree-6 vertexes). Further, it is not clear in which direction the symmetry axis would be pointing as well as how the hexagonal symmetry could be investigated form an experimental point of view. Therefore, we have considered averaged energies and stress tensors obliterating the hexagonal symmetry. In the future less heuristic averaging approaches, e.g. including stochasticity, should be considered.

Further, we had to introduce a small regularisation parameter η to guarantee boundness of steric interaction energies, as well consider Taylor-expansions of pair-interaction energies, which otherwise could "explode" at finite interaction lengths. These regularisations are necessary to follow the rigorous approach of Alicandro and Cicalese (2004) proving convergence of the microscopic model to the macroscopic model. Disregarding these regularisations the approach is only a formal one. It yields a macroscopic model based on a microscopic model, but it cannot be guaranteed that minimisers of the microscopic model indeed converge to minimisers of the macroscopic model, which is non-trivial (Friesecke and Theil 2002). Our approach should be generalised in the future, such that these regularisations could be lifted.

The derived model has been challenged by a quantitative comparison with a typical biophysical experiment: an optical tweezers experiment. To perform an optical tweezers experiment in silico, we have developed an appropriate finite element scheme, which can handle mechanics on a hypersurface and bulk mechanics including their coupling within one scheme. Simulation results show a good qualitative and quantitative agreement with experiments (Hénon et al. 1999) and simulations of the microscopic model (Li et al. 2005) (see Fig. 7). The developed numerical approach based on the toolbox GASCOIGNE (Becker et al. 2009) is much more flexible than many schemes available, e.g. boundary element methods (Pozrikidis 2003a). It can be easily extended to more complicated models, e.g. models considering interactions between mechanics and biochemistry in the cytosol and membrane at the same time, making it a powerful tool for the theoretical investigation of the mechanobiology of single cells.

Since we have found a good qualitative and quantitative agreement between microscopic simulations and the derived macroscopic continuum model, our approach could be used for parameter estimation in the near future. Parameter estimation together with the multiscale approach, allowing a

significant speedup of simulations, would enable us to estimate microscopic mechanical parameters through upscaling. Thus the microscopic model of spectrin relying on the worm-like chain model originally introduced for DNA could be improved. Hence the experimental results could be better approximated by the microscopic model and therefore also by the derived macroscopic continuum model, which is approximating the microscopic one.

The extension of mathematical multiscale techniques and the development of a highly flexible computational framework for single cell mechanics offers the possibility to tackle many unsolved questions in the field of mechanobiology in the near future. We believe that these techniques will have a significant impact on modelling in mechanobiology, as underlined by the test cases of RBC mechanics.

Acknowledgments This work was part of a Doctoral Thesis (Hartmann 2007) supervised by Prof. Willi Jäger and Prof. Marek Niezgódka. The author would like to thank them both for their support. Further, the author thanks Prof. Andrey Piatnitski and Dr. Mariya Pytashnik for very stimulating discussions, as well as Dr. Dominik Meidner and Dr. Thomas Richter for their outstanding GASCOIGNE support. Visualisations in this article are based on the visualisation toolkits VISUSIMPLE (http://www.visusimple.uni-hd.de) and PARAVIEW (http://www.paraview.org).

Appendix: Interaction lengths and invariants

The tensor $(\mathbf{F}^\Gamma)^T \cdot \mathbf{F}^\Gamma$ considered in Sect. 3.4 is symmetric and positive definite, hence it can be diagonalised:

$$(\mathbf{F}^\Gamma)^T \cdot \mathbf{F}^\Gamma = \mathbf{\Phi}^T \cdot \mathbf{\Lambda} \cdot \mathbf{\Phi}$$

with

$$\mathbf{\Lambda} = \operatorname{diag}\left(1 + \frac{I_2+\sqrt{I_2^2+4I_2-4I_1^2-8I_1}}{2}, 1 + \frac{I_2-\sqrt{I_2^2+4I_2-4I_1^2-8I_1}}{2}, 0\right)$$

and an appropriate transformation $\mathbf{\Phi}$, i.e. a rotation with an angle ϕ. I_1 and I_2 are the invariants given in (17). Hence, we obtain

$$\boldsymbol{\xi}_i^T \cdot \boldsymbol{F}^T \cdot \boldsymbol{F} \cdot \boldsymbol{\xi}_i - 1 = (\mathbf{\Phi} \cdot \boldsymbol{\xi}_i)^T \cdot (\mathbf{\Lambda} - \mathbf{1}) \cdot (\mathbf{\Phi} \cdot \boldsymbol{\xi}_i),$$

and thus, c.f. Taylor expansion (16):

$$\sum_{i=1,\dots,6} \left(\boldsymbol{\xi}_i^T \cdot \boldsymbol{F}^T \cdot \boldsymbol{F} \cdot \boldsymbol{\xi}_i - 1\right) = 3I_2,$$

$$\sum_{i=1,\dots,6} \left(\boldsymbol{\xi}_i^T \cdot \boldsymbol{F}^T \cdot \boldsymbol{F} \cdot \boldsymbol{\xi}_i - 1\right)^2 = \frac{3}{4}(4I_2 - 8I_1 + 3I_2^2 - 4I_1^2),$$

$$\sum_{i=1,\dots,6} \left(\boldsymbol{\xi}_i^T \cdot \boldsymbol{F}^T \cdot \boldsymbol{F} \cdot \boldsymbol{\xi}_i - 1\right)^3 = \frac{3}{8}I_2(12I_2 + 5I_2^2 - 12I_1^2 - 24I_1) + \frac{3}{16}(I_2^2 + 4I_2 - 4I_1^2 - 8I_1)^{3/2}\cos(6\phi),$$

i.e. the hexagonal structure of the network is reflected in the terms $(\boldsymbol{\xi}_i^T \cdot \boldsymbol{F}^T \cdot \boldsymbol{F} \cdot \boldsymbol{\xi}_i - 1)^j$ with $j <= 2$, since these terms depend only on the invariants I_1 and I_2.

Since the direction of a symmetry axis is not distinguished, we consider the following averaged and thus isotropic terms for $p > 2$:

$$\int_0^{2\pi} \sum_{i=1,\dots,6} \left(\boldsymbol{\xi}_i^T \cdot \boldsymbol{F}^T \cdot \boldsymbol{F} \cdot \boldsymbol{\xi}_i - 1\right)^3 \mathrm{d}\phi = \frac{3}{8}I_2(12I_2 + 5I_2^2 - 12I_1^2 - 24I_1),$$

$$\int_0^{2\pi} \sum_{i=1,\dots,6} \left(\boldsymbol{\xi}_i^T \cdot \boldsymbol{F}^T \cdot \boldsymbol{F} \cdot \boldsymbol{\xi}_i - 1\right)^4 \mathrm{d}\phi = \frac{3}{64}(192I_1^3 + 48I_1^4 - 240I_2^2 I_1 - 120I_2^2 I_1^2 + 35I_2^4 + 192I_1^2 + 48I_2^2 - 192I_2 I_1 - 96I_2 I_1^2 + 120I_2^3).$$

References

Alicandro R, Cicalese M (2004) A general integral representation result for continuum limits of discrete energies with superlinear growth. SIAM J Appl Math 36:1–37

Alt HW (2002) Lineare Funktionalanalysis, 4th edn. Springer, Berlin

Becker R, Braack M, Dunne T, Meidner D, Richter T, Schmich M, Stricker T, Vexler B (2009) GASCOIGNE 3D—a finite element toolbox. http://www.gascoigne.uni-hd.de

Berezhnyy M, Berlyand L (2006) Continuum limit for three-dimensional mass-spring networks and discrete Korn's inequality. J Mech Phys Solids 54:635–669

Boal D (2002) Mechanics of the cell. Cambridge University Press, Cambridge

Boey SK, Boal DH, Discher DE (1998) Simulations of the erythrocyte cytoskeleton at large deformation. I. Microscopic models. Biophys J 75:1573–1583

Bozic B, Svetina S, Zeksand B, Waugh RE (1992) Role of lamellar membrane structure in tether formation from bilayer vesicles. Biophys J 61:963–973

Braides A (2001) From discrete to continuous variational problems: an introduction. Lecture notes, School on homogenization techniques and asymptotic methods for problems with multiple scales

Braides A (2002) Γ-convergence for beginners. Oxford University Press, Oxford

Braides A, Defranceschi (1998) Homogenization of multiple integrals. Oxford University Press, Oxford

Canham P (1970) The minimum energy of bending as a possible explanation of the biconcave shape of the human red blood cell. J Theor Biol 26:61–81

Clarenz U, Diewald U, Dziuk G, Rumpf M, Rusu R (2004) A finite element method for surface restoration with smooth boundary conditions. Comput Aided Geom Des 21:427–445

Dacorogna B (2004) Introduction to the calculus of variations. Imperial College Press, London

Dal Maso G (1993) An Introduction to Γ-convergence. Birkhäuser, Boston

Dao M, Lim C, Suresh S (2003) Mechanics of the human red blood cell deformed by optical tweezers. J Mech Phys Solids 51:2259–2280

Dao M, Li J, Suresh S (2006) Molecularly based analysis of deformation of spectrin network and human erythrocyte. Math Sci Eng C 26:1232–1244

den Otter WK, Briels WJ (2003) The bending rigidity of an amphiphilic bilayer from equilibrium and nonequilibrium molecular dynamics. J Chem Phys 118:4712–4720

Discher DE, Boal DH, Boey SK (1998) Simulations of the erythrocyte cytoskeleton at large deformation. II. Micropipette aspiration. Biophys J 75:1584–1597

Evans EA, Skalak R (1980) Mechanics and thermal dynamics of biomembranes. CRC Press, Boca Raton

Friesecke G, Theil F (2002) Validity and failure of the Cauchy-Born hypothesis in a two-dimensional mass-spring lattice. J Nonlinear Sci 12:445–478

Gov NS, Safran SA (2005) Red blood cell membrane fluctuations and shape controlled by ATP-induced cytoskeletal defects. Biophys J 88:1859–1874

Hansen JC, Skalak R, Chien S, Hoger A (1997) Influence of network topology on the elasticity of the red blood cell membrane skeleton. Biophys J 72:2369–2381

Hartmann D (2007) Multiscale modelling, analysis, and simulation in mechanobiology. Doctor of Sciences, Department of Mathematics and Computer Sciences, University of Heidelberg

Heinrich V, Waugh RE (1996) A piconewton force transducer and its application to measurement of the bending stiffness of phospholipid membranes. Ann Biomed Eng 24:595–605

Helfrich W (1973) Elastic properties of lipid bilayers: Theory and possible experiments. Z Naturforsch C 28:693–703

Hénon S, Lenormand G, Richert A, Gallet F (1999) A new determination of the shear modulus of the human erythrocyte membrane using optical tweezers. Biophys J 76:1145–1151

Hwangand WC, Waugh RE (1997) Energy of dissociation of lipid bilayer from the membrane skeleton of red blood cells. Biophys J 72:2669–2678

Ingber DE (2003) Tensegrity I. Cell structure and hierarchical systems biology. J. Cell Sci. 116:1157–1173

Kuzman D, Svetina S, Waugh RE, Zeks B (2004) Elastic properties of the red blood cell membrane that determine echinocyte deformability. Eur Biophys J 33:1–15

Lee JCM, Wong DT, Discher DE (1999) Direct measures of large, anisotropic strains in deformation of the erythrocyte cytoskeleton. Biophys J 77:853–864

Lenormand G, Hénon S, Richert A, Simeon J, Gallet F (2001) Direct measurement of the area expansion and shear moduli of the human red blood cell membrane skeleton. Biophys J 81:43–56

Li J, Dao M, Lim CT, Suresh S (2005) Spectrin-level modeling of the cytoskeleton and optical tweezers stretching of the erythrocyte. Biophys J 88:3707–3719

Lim GHW, Wortis M, Mukhopadhyay R (2002) Stomatocyte discocyte echinocyte sequence of the human red blood cell: Evidence for the bilayer couple hypothesis from membrane mechanics. Proc Natl Acad Sci USA 99:16,766–16,769

Liu S, Derick LH, Palek J (1987) Visualization of the hexagonal lattice in the erythrocyte membrane skeleton. J Cell Biol 104:527–536

Marko J, Siggia ED (1995) Stretching DNA. Macromolecules 28: 8759–8770

Miao L, Seifert W, Wortis M, Döbereiner HG (1994) Nbudding transitions of fluid-bilayer vesicles: The effect of area-difference elasticity. Phys Rev E 49:5389–5407

Mills JP, Qie L, Dao M, Lim CT, Suresh S (2004) Nonlinear elastic and viscoelastic deformation of the human red blood cell with optical tweezers. Mech Chem Biosys 1:169–180

Mohandas N, Evans E (1994) Mechanical properties of the red cell membrane in relation to molecular structure and genetic defects. Annu Rev Biophys Biom 23:787–818

Mukhopadhyay R, Lim GHW, Wortis M (2002) Echinocyte shapes: bending, stretching, and shear determine spicule shape and spacing. Biophys J 82:1756–1772

Noguchi H, Gompper G (2005) Shape transitions of fluid vesicles and red blood cells in capillary flows. Proc Natl Acad Sci USA 102:14,159–14,164

Pozrikidis C (2003a) Numerical simulation of the flow-induced deformation of red blood cells. Ann Biomed Eng 31:1194–1205

Pozrikidis C (2003b) Modeling and simulation of capsules and biological cells. CRC Press, Boca Raton

Rannacher R (2006) Numerische Mathematik 3: Numerische Methoden für Probleme der Kontinuumsmechanik. Lecture notes

Rawicz W, Olbrich KC, McIntosh T, Needham D, Evans E (2000) Effect of chain length and unsaturation on elasticity of lipid bilayers. Biophys J 79:328–339

Rusu RE (2005) An algorithm for the elastic flow of surfaces. Interface. Free Bound. 7:229–239

Scheffer L, Bitler A, Ben-Jacob E, Korenstein R (2001) Atomic force pulling: Probing the local elasticity of the cell membrane. Eur Biophys J 30:83–90

Schmidt B (2008) On the passage from atomic to continuum theory for thin films. Arch Ration Mech An 190:1–55

Seifert U, Berndl K, Lipowsky R (1991) Shape transformations of vesicles: Phase diagram for spontaneous-curvature and bilayer-coupling models. Phys Rev A 44:1182–1202

Skalak R, Tözeren A, Zarda PR, Chien S (1973) Strain energy function of red blood cell membranes. Biophys J 13:245–264

Steltenkamp S, Müller MM, Deserno M, Hennesthal C, Steinem C, Janshoff A (2006) Mechanical properties of pore-spanning lipid bilayers probed by atomic force microscopy. Biophys J 91:217–226

Thompson D (1917) On growth and form (Abr. ed. by J. T. Bonner, 1961). Cambridge University Press, Cambridge

Willmore TJ (1993) Riemannian geometry. Clarendon Press, Oxford